THESIS FOR THE DEGREE OF LICENTIATE OF ENGINEERING

Active magnetoplasmonics

for nanoscale distances sensing

IRINA ZUBRITSKAYA

Department of Applied Physics

CHALMERS UNIVERSITY OF TECHNOLOGY

Göteborg, Sweden 2015

Active magnetoplasmonics
for nanoscale distances sensing

IRINA ZUBRITSKAYA

© IRINA ZUBRITSKAYA, 2015

Department of Applied Physics
Chalmers University of Technology
SE-412 96 Göteborg
Sweden
Telephone +46 (0)317721000

Cover:
Magnetoplasmonic ruler based on array of dimer nanoantennas

Chalmers reproservice
Göteborg, Sweden 2015

Active magnetoplasmonics for nanoscale distances sensing

Irina Zubritskaya
Department of Applied Physics
Chalmers University of Technology

Abstract

Magnetoplasmonics is an emerging field within nano-photonics that operates with the combination of propagating or localized surface plasmons and magnetism. Active and adaptive magnetoplasmonic components that are capable of controlling light on the nanoscale with external weak magnetic fields are envisioned to push the development of integrated photonic circuits, high-density data storage, or the advanced schemes for bio- and chemo-sensing. In these components plasmon-enhanced and controlled magneto-optical activity creates a new way of active control of plasmonic devices.

In this thesis we investigate the role of localized surface plasmons on magneto-optical activity and demonstrate how magnetoplasmonics can be employed in the optical detection of nanoscale distances. Plasmon rulers are an emerging concept in which the strong near-field coupling of plasmon nanoantenna elements is employed to obtain structural information at the nanoscale. We introduce an active magnetoplasmonic ruler that provides active operation and nanoscale distances reading with the figure-of-merit substantially exceeding the one of traditional plasmon rulers. We combine nanoplasmonics and nanomagnetism to conceptualize a magnetoplasmonic dimer nanoantenna that would be able to report nanoscale distances while optimizing its own spatial orientation. The latter constitutes an active operation, in which a dynamically optimized optical response per measured unit length allows for the measurement of small and large nanoscale distances with about two orders of magnitude higher precision than current state-of-the-art plasmon rulers.

Keywords: magnetoplasmonics, plasmon ruler, nickel, cobalt, localized surface plasmon resonance, magneto-optical Kerr effect (MOKE), dimer.

APPENDED PAPERS

The following papers are included in this thesis:

Paper: *Active magnetoplasmonic ruler.*
Zubritskaya, I.; Lodewijks, K.; Maccaferri, N.; Mekonnen, A.; Dumas, R. K.; Åkerman, J.; Vavassori, P.; Dmitriev, A. *Nano Letters* **2015,** 15, (5), 3204-11.

My contribution: I contributed to devising a concept, performed all nanofabrication, optical and MOKE experimental measurements, wrote first version of the manuscript.

Works, not included in this thesis:

Paper: Magnetoplasmonic design rules for active magneto-optics.
Lodewijks, K.; Maccaferri, N.; Pakizeh, T.; Dumas, R. K.; Zubritskaya, I.; Akerman, J.; Vavassori, P.; Dmitriev, A. *Nano Letters* **2014,** 14, (12), 7207-14.

Conference proceeding:
Magnetoplasmonic design rules for active magneto-optics,
Lodewijks, K.; Maccaferri, N.; Pakizeh, T.; Dumas, R. K.; Zubritskaya, I.; Akerman, J.; Vavassori, P.; Dmitriev, A., ImagineNano 2015 - PPM Conference, Bilbao, Spain.

Contents

Chapter 1

1 Why magnetoplasmonics?

Surface plasmons are electromagnetic waves coupled to the collective oscillations of the free surface charges, strongly localized at an interface between two media with permittivities with opposite sign, typically a dielectric and a metal. They can exist either in a form of localized surface plasmons in nanoparticles, or as surface plasmon polaritons, also known as propagating plasmons, supported by planar interfaces. Plasmonics, being a major part of nanophotonics, is a research field that studies the phenomena and applications associated with surface plasmons [1-3], which was established around the turn of 20th century. *Magnetoplasmonics* is a relatively young but extensively growing field, which merges plasmonics and magnetism to devise conceptually new functionalities [4, 5]. The investigation of the phenomena arising from the mutual interplay between magnetism and light-matter interactions in spatially confined geometries became a hot topic owing to the recent advances in nanotechnology. The research route of magnetoplasmonics is twofold: controlling the plasmon properties with magnetic field on one hand and controlling the magneto-optical properties with plasmons on the other hand. The first route mainly focuses on the modulation of propagating surface plasmons with magnetic field. It was in early '70s when the effect of magnetic field on plasmons was first analyzed on structures made of highly doped semiconductors and metals supporting propagating plasmons in far-infrared region. The idea to control the properties of plasmons, such as propagation and localization, became very appealing for the development of new active devices; however, too high magnetic fields, required for the proper control of the plasmon wave vector, hindered it from realization in real applications. Nanoengineering of new systems made from ferromagnetic materials and noble metals made it possible to control the plasmon wave vector with weak external magnetic field [6, 7] and generate ultrashort surface plasmon polariton pulses [8, 9]. Magnetic manipulation of propagating plasmons in magnetoplasmonic crystals, leading to the enhancement of magneto-optical activity and magneto-optical transparency [10], makes these systems suitable for applications in telecommunications, magnetic sensing and all-optical magnetic data storage. Another topic in magnetoplasmonics is the localized surface plasmons in purely magnetic or

combined magnetic-noble metal systems. In contrast to heavily damped propagating plasmons in magnetic materials, localized plasmons have strong effects on magneto-optical activity due to the huge local field enhancement in spatially confined nanostructures. As a consequence, strongly enhanced magneto-optical activity [11] and tunability of magneto-optical response [12, 13] can be achieved with localized plasmons. Plasmon-enhanced and controlled magneto-optical activity creates a new way of active control of plasmonic devices by the weak magnetic fields.
One of practical applications, where magnetoplasmonics becomes eminent, is thermally-assisted magnetic recording, where the integration of a plasmonic antenna into a magnetic recording head was shown to dramatically improve the storage density up to ~1 Tb/inch^2 [14]. A very recent work demonstrated the utilization of plasmon-tunable magneto-optical activity in magnetoplasmonic nanostructures in conceptually new scheme of ultrasensitive bio-detection [15].

Active and adaptive magnetoplasmonic components, capable of controlling light on the nanoscale with external magnetic fields, are required for the development of integrated photonic circuits in telecommunications, for high-density data storage, or in advanced schemes for bio- and chemo-sensing, to name a few. In this thesis I investigate the role of localized surface plasmons on magneto-optical activity and demonstrate how magnetoplasmonics can be employed in the optical detection of nanoscale distances. I introduce a concept of an active magnetoplasmonic ruler [16], providing active operation and nanoscale distances reading with the figure-of-merit substantially exceeding the one of traditional plasmon rulers.

Chapter 2

2 Plasmonic nanoparticles

Chapter 2 is focusing on plasmonics and describes the physics behind localized surface plasmon resonances in nanoparticles. In section 2.1 I describe the optical properties of metals and provide the theoretical background of electromagnetics of metals in terms of classical electrodynamics based on Maxwell's equations. The role of dielectric function in optical properties of metals is explained. In section 2.2 I introduce localized plasmons in metal nanoparticles and provide the analytical expressions for the polarizability of sub-wavelength nanoparticles and also beyond the quasi-static approximation. I close this chapter by describing the effects of plasmon coupling on optical properties of nanoparticle dimers.

2.1 Optical properties of metals

The interaction of metals with electromagnetic fields is frequency-dependent. At microwave and far-infrared frequencies metals are highly reflective and do not allow the propagation of electromagnetic waves. The field penetration increases significantly at higher frequencies in near-infrared and visible parts of the spectrum. Electromagnetic fields with frequencies in ultraviolet region of the spectrum can penetrate into and propagate through the metals. Frequency-dependent character of optical response is closely related to the dispersive properties of the complex dielectric function $\varepsilon(\omega)$ and conductivity $\sigma(\omega)$.

2.1.1 Theoretical foundations of macroscopic electrodynamics

The optical properties of metals can be described in terms of classical electrodynamics based on Maxwell's equations. Maxwell's equations together with the Lorentz force law summarize the entire theoretical contest of classical electrodynamics and optics and tell how charges and currents generate fields and, reciprocally, how fields affect charges [17-19]:

$$\nabla \cdot E = \frac{1}{\varepsilon_0}\rho_{ext} \qquad (Gauss's\ law) \tag{1}$$

$$\nabla \cdot B = 0 \tag{2}$$

$$\nabla \times E = -\frac{\partial B}{\partial t} \qquad (Faraday's\ law) \tag{3}$$

$$\nabla \times B = \mu_0 J_{ext} + \mu_0 \varepsilon_0 \frac{\partial E}{\partial t} \qquad (Ampère's\ law\ with\ Maxwell's\ correction) \tag{4}$$

$$F = q\,(E + v \times B), \qquad (Lorentz\ force\ law) \tag{5}$$

where E denotes the electric field, B is the magnetic induction or magnetic flux density, J_{ext} and ρ_{ext} are the external current and charge densities, q is the electric charge, v is the velocity, ε_0 and μ_0 are the dielectric permittivity and the magnetic permeability of vacuum[1]. The continuity equation

$$\nabla \cdot J = -\frac{\partial \rho}{\partial t} \qquad (Continuity\ equation) \tag{6}$$

is the mathematical expression of conservation of charge and is built in Maxwell's equation. It can be derived by taking the divergence of Ampère's law [17],[18].

Constitutive relations display the material properties and show how it behaves under the influence of the fields. For non-dispersive linear[2] and isotropic[3] medium

$$D = \varepsilon\varepsilon_0 E \qquad (P = \varepsilon_0 \chi_e\, E) \tag{7}$$

$$H = \frac{1}{\mu\mu_0} B \qquad (M = \chi_m H) \tag{8}$$

$$J = \sigma E, \tag{9}$$

[1] $\varepsilon_0 \approx 8.854 \times 10^{-12}\ F/m$ and $\mu_0 \approx 1.257 \times 10^{-6}\ H/m$

[2] In non-linear medium the polarization P is described by a Taylor series expansion and include the terms of higher power of E

[3] In anisotropic media ε and μ together with χ_e and χ_m are second-rank tensors:
$\vec{\vec{\varepsilon}} = \varepsilon_0(\tilde{I} + \vec{\vec{\chi_e}})$ and $\vec{\vec{\mu}} = \mu_0(\tilde{I} + \vec{\vec{\chi_m}})$, $\tilde{I}$ is identity matrix

where the dielectric displacement D, polarization P, the internal conduction current density J induced by the magnetization M, and the magnetic field H are expressed in terms of E and B with the conductivity σ and dielectric permittivity ε and magnetic permeability μ, which depend on the nature of the material and connected with electric and magnetic susceptibility χ_e and χ_m through the relations:

$$\varepsilon = \varepsilon_0(1 + \chi_e) \tag{10}$$

$$\mu = \mu_0(1 + \chi_m). \tag{11}$$

Importantly, Maxwell's and other equations in this section are written in their macroscopic form, which uses charge densities and current densities instead of total charge and total current. The microscopic properties of matter and microscopic fields can be included in Maxwell's equations by considering charges and currents at the atomic scale.

An electromagnetic time-dependent field in a linear medium can be written as a superposition of monochromatic plane-wave components [1, 18]

$$E(r,t) = E(k,\omega)\cos(k \cdot r - \omega t). \tag{12}$$

Therefore the induced dielectric displacement $D(r,t)$ and the internal conduction current $J(r,t)$ can be rewritten as [1, 18]

$$D(k,\omega) = \varepsilon_0 \varepsilon(k,\omega) E(k,\omega) \tag{13}$$

$$J(k,\omega) = \sigma(k,\omega) E(k,\omega), \tag{14}$$

were k and ω are the wavevector and the angular frequency. Since $E(k,\omega)$ is equivalent to the Fourier transform $\hat{E}$ of the time-dependent field $E(r,t)$, the inverse Fourier transform can be applied to equations (13) and (14) and the constitutive relations (7) and (9) can be rewritten in a general form taking into account the *non-locality* of the medium in time and space [18]:

$$D(r,t) = \varepsilon_0 \iint \tilde{\varepsilon}(r - r', t - t') E(r', t') dr' dt' \tag{15}$$

$$J_c(r,t) = \iint \tilde{\sigma}(r-r', t-t')E(r',t')dr'dt'. \tag{16}$$

In a *non-local* medium the displacement D and the conduction current J_c at time t depend on the electric field E at all times t' previous to time t, which referred to as *temporal dispersion*. Similarly, if the displacement D and the conduction current J_c at a point r depend on the electric field E at all neighboring points r', the medium is called *spatially dispersive* or *non-local*. While spatial dispersion is a very weak effect, the temporal dispersion is a widely encountered phenomenon and should be taken into account.

Spectral representation of time-dependent fields is given by Fourier transform and the spectrum $\hat{E}(r,\omega)$ of a time-dependent field $E(r,t)$ is defined as

$$\hat{E}(r,\omega) = \frac{1}{2\pi}\int_{\infty}^{-\infty} E(r,t)e^{i\omega t}dt. \tag{17}$$

The solution of Maxwell's equations in Fourier (frequency) domain $\hat{E}(r,\omega)$ can be found by applying Fourier transform to Maxwell's equations in time domain and making a substitution $\frac{\partial}{\partial t} \to -i\omega$. Together with constitutive relations (7) and (8) the substitution Maxwell's equations in Fourier domain will have a form:

$$\nabla \cdot \hat{D}(r,\omega) = \hat{\rho}_{ext}(r,\omega) \tag{18}$$

$$\nabla \cdot \hat{B}(r,\omega) = 0 \tag{19}$$

$$\nabla \times \hat{E}(r,\omega) = i\omega\hat{B}(r,\omega) \tag{20}$$

$$\nabla \times \hat{H}(r,\omega) = \hat{J}_{ext}(r,\omega) - \omega\hat{D}(r,\omega), \tag{21}$$

where the solution $\hat{E}(r,\omega)$ in frequency domain and the solution $E(r,t)$ in time domain are related through the inverse Fourier transform as

$$\hat{E}(r,t) = \int_{\infty}^{-\infty} \hat{E}(r,\omega)e^{-i\omega t}dt. \tag{22}$$

We rewrite the equations (13) and (14) by replacing $D(k,\omega)$ and $J(k,\omega)$ with $D = \varepsilon_0 E + P$ and $J = \frac{\partial P}{\partial t}$, where the latter comes from the relationships $\nabla \cdot P = -\rho$ and the conservation of charge $\nabla \cdot J = -\frac{\partial \rho}{\partial t}$:

$$\varepsilon_0 E(k,\omega) + P = \varepsilon_0 \varepsilon(k,\omega) E(k,\omega) \tag{23}$$

$$\frac{\partial P}{\partial t} = \sigma(k,\omega) E(k,\omega). \tag{24}$$

Finally, the fundamental relationship between the dielectric permittivity (dielectric function) $\varepsilon(k,\omega)$ and the conductivity $\sigma(k,\omega)$ can be found by making a replacement $\frac{\partial}{\partial t} \to -i\omega$ and expressing $\varepsilon(k,\omega)$ through $\sigma(k,\omega)$ [1]:

$$\varepsilon(k,\omega) = 1 + \frac{i\sigma(k,\omega)}{\varepsilon_0 \omega}. \tag{25}$$

This relationship can be simplified by assuming that ε is only the function of the frequency and not the wavevector, i.e. $\varepsilon(k=0,\omega) = \varepsilon(\omega)$, which is true for up to ultraviolet frequencies [1]:

$$\varepsilon(\omega) = 1 + \frac{i\sigma(\omega)}{\varepsilon_0 \omega}. \tag{26}$$

Both the dielectric function

$$\varepsilon(\omega) = \varepsilon_1 + i\varepsilon_2$$

and the conductivity

$$\sigma(\omega) = \sigma_1 + i\sigma_2$$

have their real and imaginary parts and are complex functions of the frequency ω. The optical properties of metals are described by the complex dielectric function $\varepsilon(\omega)$ with imaginary part $\varepsilon_2(\omega)$ that is responsible for light absorption and energy dissipation associated with the motion of free electrons in metals.

2.1.2 Dielectric function of metals

Plasma model can be used over a wide range of frequencies to describe the optical properties of metals. According to the free-electron model, free conduction electrons oscillate against the fixed ion lattice 180° out of phase relative to the driving electromagnetic field. The motion of free electrons is damped via collisions that occur with characteristic collision frequency $\gamma = {}^{1}/_{\tau}$, where τ is relaxation time of free electron gas. At room temperature $\tau \sim 10^{-14}$, which results in $\gamma \sim 100$ THz. According to Drude-Sommerfeld theory, the equation of motion of a free electron with mass m and charge e in external electric field E can be written as [1]

$$m\ddot{x} + m\gamma\dot{x} = -eE. \tag{1}$$

For harmonic time dependence of the driving field $E(t) = E_0 e^{-i\omega t}$ a particular solution of the equation describing the oscillation of the electron $x(t) = x_0 e^{-i\omega t}$ is used to find that

$$x(t) = \frac{e}{m(\omega^2 - i\gamma\omega)} E(t). \tag{2}$$

The displaced electrons of density n contribute to a macroscopic polarization $P = -nex$, or

$$P(t) = -\frac{ne^2}{m(\omega^2 - i\gamma\omega)} E(t). \tag{3}$$

We insert this expression into $D = \varepsilon_0 E + P$ and obtain that

$$D = \varepsilon_0 \left(1 - \frac{\omega_p^2}{\omega^2 + i\gamma\omega}\right) E, \tag{4}$$

where

$$\omega_p^2 = \frac{ne^2}{\varepsilon_0 m}$$

is the *plasma frequency* of the free-electron gas. Since $D = \varepsilon\varepsilon_0 E$, the dielectric function of the free electron gas is given by

$$\varepsilon(\omega) = 1 - \frac{\omega_p^2}{\omega^2 + i\gamma\omega}. \tag{5}$$

The complex dielectric function ε consists of real and imaginary parts:

$$\varepsilon_1(\omega) = 1 - \frac{\omega_p^2 \tau^2}{1 + \omega^2 \tau^2} \tag{6}$$

$$\varepsilon_2(\omega) = 1 - \frac{\omega_p^2 \tau}{\omega(1 + \omega^2 \tau^2)}, \tag{7}$$

where $\gamma = {}^{1}/_{\tau}$ indicates damping due to the collisions.
For large frequencies close to ω_p, the product $\omega\tau \gg 1$ resulting in predominantly real dielectric function

$$\varepsilon(\omega) = 1 - \frac{\omega_p^2}{\omega^2}, \tag{8}$$

which is known as the dielectric function of undamped free electron plasma [1]. In reality the optical response of noble metals (e.g. Au, Ag, Cu) in frequency region $\omega > \omega_p$ is highly affected by interband transitions, which are not included in Drude-Sommerfeld model and will be discussed in the next section. In low frequency regime, $\omega \ll \tau^{-1}$ which results in $\varepsilon_2(\omega) \gg \varepsilon_1(\omega)$ and metals are mainly absorbing [1].

2.1.3 Interband transitions in noble metals

At visible and higher frequencies the optical response of noble metals is determined by the transitions between the electronic bands. Interband transitions occur if photon energy exceeds the bandgap energy and bound electrons from lower-lying bands get into the conduction band. The dielectric function of interband transitions describing the contribution of bound electrons is given by [18]:

$$\varepsilon_{Interband}(\omega) = 1 + \frac{\tilde{\omega}_p^2}{(\omega_0^2 - \omega^2) - i\gamma\omega}, \tag{1}$$

where γ describes radiative damping in case of bound electrons. Here the frequency

$$\tilde{\omega}_p = \sqrt{\frac{\tilde{n}e^2}{m\varepsilon_0}}$$

has a different physical meaning than plasma frequency in plasma model with $\tilde{n}$ and m being the density and the effective mass of the bound electrons, and

$$\omega_0 = \sqrt{\frac{\alpha}{m}},$$

where α is the spring constant of the potential which keeps the electrons tied to the ion cores.

For visible and higher frequencies, the imaginary part of this dielectric function $\varepsilon_{Interband}(\omega)$ does not follow the Drude-Sommerfeld model in noble metals and resonantly increases due to interband transitions, which results in strong absorption [20]. As an alternative, the optical response of real metals in the frequency region $\omega > \omega_p$ can be described by a dielectric function, which accounts for the effect of all higher-energy interband transitions via a constant offset ε_∞ and given by

$$\varepsilon(\omega) = \varepsilon_\infty - \frac{\omega_p^2}{\omega^2 + i\gamma\omega}. \quad (2)$$

The dielectric constant ε_∞ (usually $1 \leq \varepsilon_\infty \leq 10$) describes highly polarized environment created by the filled *d* band located close to the Fermi level [1].

2.2 Localized surface plasmons

Localized surface plasmons are collective oscillations of free electron density in metallic nanostructures at the interface between a metal and a dielectric. According to the simple Drude model, the electron cloud of free conduction electrons oscillates 180° out of phase relative to the driving electric field (Fig. 2.1a). The effective restoring force, originating from the positively charged ion lattice, is exerted on the conduction electrons so that a resonance can arise, leading to field enhancement both inside and in the near-field zone outside the particle [1].

Resonantly enhanced absorption and scattering in gold and silver nanoparticles falls into the visible region of the electromagnetic spectrum, which explains bright colors observed in transmitted and reflected light. This phenomenon found applications in the staining of glass for windows (Fig.2.1b) and ornamental cups two thousand years ago but did not have a clear explanation for a long time. Now we know that the colors are due to the interplay of absorption and scattering in nanometer-sized gold particles embedded in glass [1, 18].

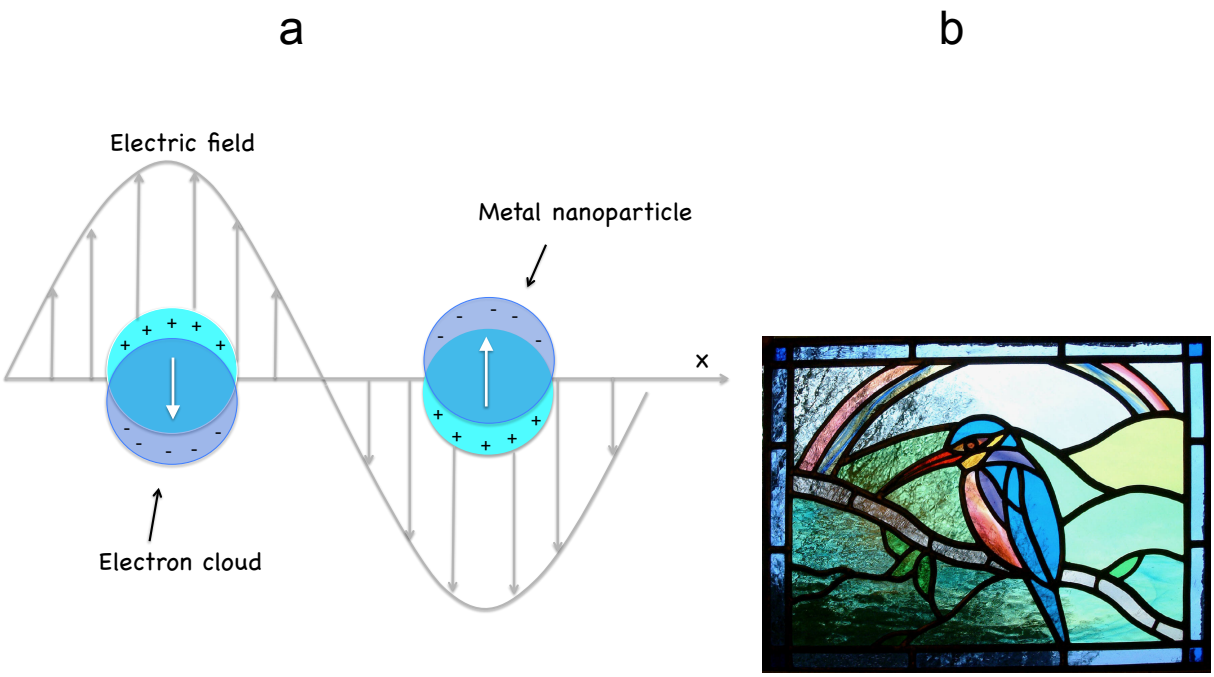

Figure 2.1. a) Illustration of dipole polarizability and oscillations of free electron density during localized plasmon resonance in metal nanoparticle. b) Kingfisher stained glass window, Worcester, UK.

2.2.1 Polarizability of a sub-wavelength metal nanoparticle

To analyze the interaction of a particle of size d with electromagnetic field one assumes that the size of the particle d is much smaller that the wavelength of light $d \ll \lambda$, and harmonically oscillating electric field $E(\omega) = E_0 e^{-i\omega t}$ is constant over the particle volume. This approach is known as *quasi-static approximation* and describes well the optical response of nanoparticles of dimensions around 100 nm and below. The harmonic time dependence $e^{-i\omega t}$ is added later when the field distribution is found. When a homogeneous metallic sphere of radius a is placed into a uniform electrostatic field (Fig. 2.2), the field induces a dipole moment inside the sphere, which is given by [1, 18]

$$p = 4\pi\varepsilon_0\varepsilon_m a^3 \frac{\varepsilon - \varepsilon_m}{\varepsilon + 2\varepsilon_m} E_0, \qquad (1)$$

where ε and ε_m are the dielectric constants of the particle and the surrounding medium, E_0 is the amplitude of the external electric field.

The polarizability α of a metallic sphere in quasi-static approximation is defined via

$$p = \varepsilon_0 \varepsilon_m \alpha E_0 \tag{2}$$

and given by

$$\alpha = 4\pi a^3 \frac{\varepsilon - \varepsilon_m}{\varepsilon + 2\varepsilon_m}. \tag{3}$$

It is clear that the polarizability in (3) experiences a resonant enhancement when $|\varepsilon + 2\varepsilon_m|$ is minimal, which in the case of small or slowly-varying $Im[\varepsilon(\omega)]$ simplifies to [1]

$$Re[\varepsilon(\omega)] = -2\varepsilon_m. \tag{4}$$

The relationship (4) is called the Fröhlich criterion and describes a *dipole surface plasmon* mode of the metal nanoparticle in a harmonically oscillating electric field $E(\omega) = E_0 e^{-i\omega t}$. For a sphere consisted of Drude metal with a dielectric function

$$\varepsilon(\omega) = 1 - \frac{\omega_p^2}{\omega^2 + i\gamma\omega},$$

located in air, the Fröhlich criterion is met at $\omega_0 = {}^{\omega_p}/_{\sqrt{3}}$. The resonance frequency ω_0 depends on the dielectric constant of the surrounding medium ε_m and the resonance redshifts as $\varepsilon_m$increases. Based on that fact, metal nanoparticles are perfectly suited for optical sensing of changes in refractive index [1].

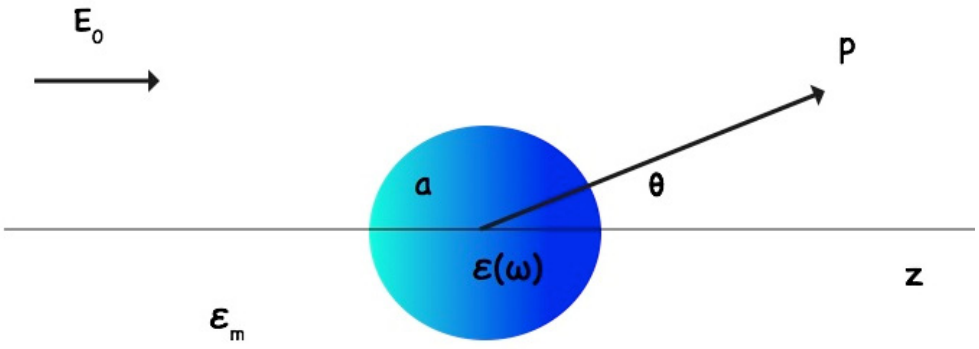

Figure 2.2. Schematics of a metal sphere in an electrostatic field.

For harmonically oscillating electric field which excites a dipole moment $p(t) = \varepsilon_0 \varepsilon_m \alpha E_0 e^{-i\omega t}$, the polarizability is given by the same expression (3) as in quasi-

electrostatic approximation. A metal nanoparticle of spherical shape at its plasmon resonance can be seen as a point dipole located in the center of the sphere. The radiation of this dipole leads to re-radiation and dissipation of the electromagnetic plane wave by the sphere [18], known as scattering and absorption, with corresponding scattering and absorption cross-sections given by [1]:

$$C_{sca} = \frac{k^4}{6\pi}|\alpha|^2 = \frac{8\pi}{3}k^4a^6\left|\frac{\varepsilon - \varepsilon_m}{\varepsilon + 2\varepsilon_m}\right|^2 \quad (5)$$

$$C_{abs} = kIm[\alpha] = 4\pi ka^3 Im\left[\frac{\varepsilon - \varepsilon_m}{\varepsilon + 2\varepsilon_m}\right]. \quad (6)$$

The important consequence of resonantly enhanced polarizability of a sub-wavelength metal nanoparticle, acting as an electric dipole, is that the nanoparticle resonantly absorbs and scatters electromagnetic fields at the dipole plasmon resonance. The extinction, the sum of absorption and scattering, depends on the particle size (Fig. 2.3), shape and the dielectric function of the surrounding medium.

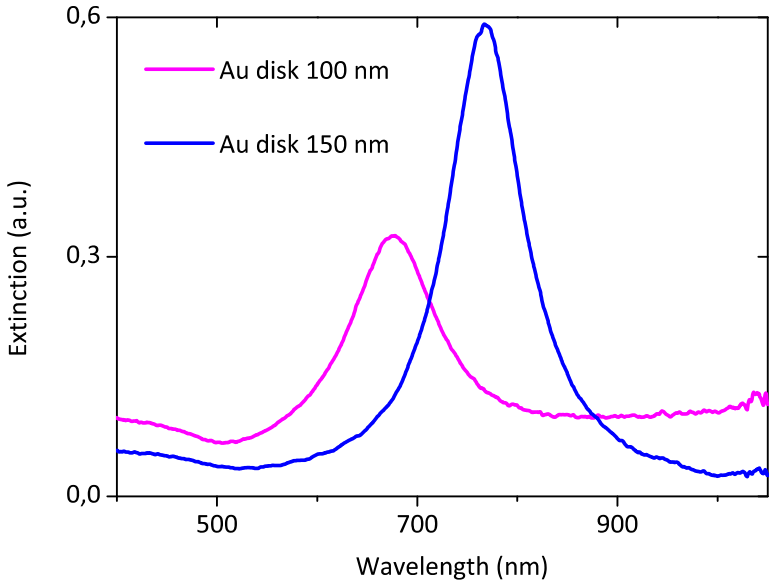

Figure 2.3. Extinction measured at around localized surface plasmon resonance in gold nanodisks with diameters 100 nm and 150 nm and thickness 30 nm. .

Although the basic physics of localized surface plasmon resonance is described on the assumption of spherical shape of the nanoparticle, the polarizability can be derived for nanoparticles with more general ellipsoid shape and is given by [1, 21]

$$\alpha_i = 4\pi a_1 a_2 a_3 \frac{\varepsilon(\omega) - \varepsilon_m}{3\varepsilon_m + 3L_i(\varepsilon(\omega) - \varepsilon_m)}, \tag{7}$$

where the semiaxes $a_1 \leq a_2 \leq a_3$ are specified by

$$\frac{x^2}{a_1^2} + \frac{y^2}{a_2^2} + \frac{z^2}{a_3^2} = 1.$$

α_i $(i = 1,2,3)$ define the polarizabilities along the principal axes of the ellipsoid. L_i are elements defined by the geometry and given by

$$L_i = \frac{a_1 a_2 a_3}{2} \int_0^\infty \frac{dq}{(a_i^2 + q) f(q)}, \tag{8}$$

where $f(q) = \sqrt{(q + a_1^2)(q + a_2^2)(q + a_3^2)}$. The elements L_i satisfy the condition $\sum L_i = 1$, and for a sphere $L_1 = L_2 = L_3 = {}^1/_3$. Alternatively, the polarizability of ellipsoids can be expressed in terms of *depolarization factors* $\widetilde{L_\iota}$, defined via $E_{1i} = E_{0i} - \widetilde{L_\iota} P_{1i}$, where $E_{1i}$and P_{1i} are the electric field and polarization induced inside the particle by the external field E_{0i} along the principal axis i. L_i and $\widetilde{L_\iota}$ are connected by the relationship

$$\widetilde{L_\iota} = \frac{\varepsilon - \varepsilon_m}{\varepsilon - 1} \frac{L_i}{\varepsilon_0 \varepsilon_m}. \tag{9}$$

Nanoparticles used in this work can be classified as a special case of ellipsoids with two major axes of the same size $a_1 = a_2$, called *oblate spheroids*. Nanoparticles of this shape exhibit two spectrally separated plasmon resonances corresponded to the oscillations of the conduction electrons along the major or the minor axes, respectively. The resonance along the major axis is significantly red-shifted compared to the resonance of a sphere of the same volume [1].

An important class of nanoparticles, which recently gained a great amount of attention in plasmonics due to their wide tunability of the resonance, is core-shell nanoparticles. The polarizability of a core-shell nanoparticle consisting of a dielectric core with $\varepsilon_1(\omega)$ and a metallic shell with $\varepsilon_2(\omega)$ is given by [21]

$$\alpha = 4\pi a_2^3 \frac{(\varepsilon_2 - \varepsilon_m)(\varepsilon_1 + 2\varepsilon_2) + f(\varepsilon_1 - \varepsilon_2)(\varepsilon_m + 2\varepsilon_2)}{(\varepsilon_2 + 2\varepsilon_m)(\varepsilon_1 + 2\varepsilon_m) + f(2\varepsilon_2 - 2\varepsilon_m)(\varepsilon_1 - \varepsilon_2)}, \tag{10}$$

where $f = {a_1^3}/{a_2^3}$, a_1 and a_2 are the inner and the outer radii, respectively.

2.2.2 Localized surface plasmon resonance beyond quasi-electrostatic limit

The results for resonantly enhanced polarizability, absorption and scattering by a sub-wavelength nanoparticle obtained in quasi-electrostatic approximation, where the nanoparticle is seen as an electric dipole, which absorbs and scatters light, is no longer valid for nanoparticles with dimensions compared to the wavelength of light. In practice, the quasi-electrostatic approximation gives reasonably good results for spherical and ellipsoidal nanoparticles with dimensions below 100 nm, illuminated by visible or near-infrared light. For larger nanoparticles, where the driving electromagnetic field is not constant over the nanoparticle volume due to the phase-changes, one uses an approach known as *Mie theory* where internal and scattered fields are expanded into a set of *normal modes*. The expansion of the first TM mode of *Mie theory* gives an expression for the polarizability of a sphere with volume V, given by [1]:

$$\alpha_{Sphere} = \frac{1 - \left(\frac{1}{10}\right)(\varepsilon + \varepsilon_m)x^2 + O(x^4)}{\left(\frac{1}{3} + \frac{\varepsilon_m}{\varepsilon - \varepsilon_m}\right) - \frac{1}{30}(\varepsilon + 10\varepsilon_m)x^2 - i\frac{4\pi^2\varepsilon_m^{3/2}}{3}\frac{V}{\lambda_0^3} + O(x^4)}, \quad (1)$$

where $x = \frac{\pi a}{\lambda_0}$ is the *size parameter,* relating the radius a to the free-space wavelength. Formula for the polarizability (1) can be generalized for ellipsoid structures, giving the polarizability along the principal axis with geometrical factor L [1]:

$$\alpha_{Ellipsoid} \approx \frac{V}{\left(L + \frac{\varepsilon_m}{\varepsilon - \varepsilon_m}\right) + A\varepsilon_m x^2 + B\varepsilon_m^2 x^4 - i\frac{4\pi^2\varepsilon_m^{3/2}}{3}\frac{V}{\lambda_0^3}}, \quad (2)$$

where the parameters A and B are the functions of L and obtained using empirical data. The term quadratic in x in the numerator includes the effect of retardation of the exciting field over the volume of the sphere. Another quadratic term in the denominator describes the effect of the retardation of the *depolarization field* inside the particle. Both effects lead to a red-shift of the resonance as the size of the particle increases, which also means that the influence of the interband transitions gets limited as the resonance shifts

towards lower energies. The imaginary term in the denominator accounts for *radiation damping,* caused by a direct radiative decay route of the coherent electron oscillations into photons [1].

There are two main mechanisms of plasmon damping beyond the electrostatic approximation in nanoparticles made of noble metals: a radiative decay into photons, dominating for larger particles, and non-radiative decay (absorption) due to the creation of electron-hole pairs via either intraband or interband transitions [1]. In ferromagnetic nanoparticles, plasmons in addition are heavily damped via thermal decay due to ohmic losses. Damping processes are responsible for a significant broadening of the plasmon resonance linewidth.

2.2.3 Localized surface plasmons coupling

The interaction between localized surface plasmon resonances of individual nanoparticles in complex structures, referred to as plasmon coupling, leads to the *hybridization* of individual plasmon modes [22]. In arrays of small nanoparticles, the electromagnetic interactions between the localized modes can in first approximation be treated as an interaction between point dipoles. This interaction is strongly dependent on the interparticle distance. For closely spaced particles with $d \ll \lambda$, near-field interactions with a distance dependence d^{-3} dominate, and the particle array can be seen as an array of point dipoles interacting via their near-field. Near-field coupling results in strongly enhanced local field in the nano-gaps between or at the intersection points of adjacent particles [1, 18], which decays as d^{-3} with distance (see Fig. 2.4). For larger particle separations, far-field dipolar coupling with a distance dependence d^{-1} dominates.

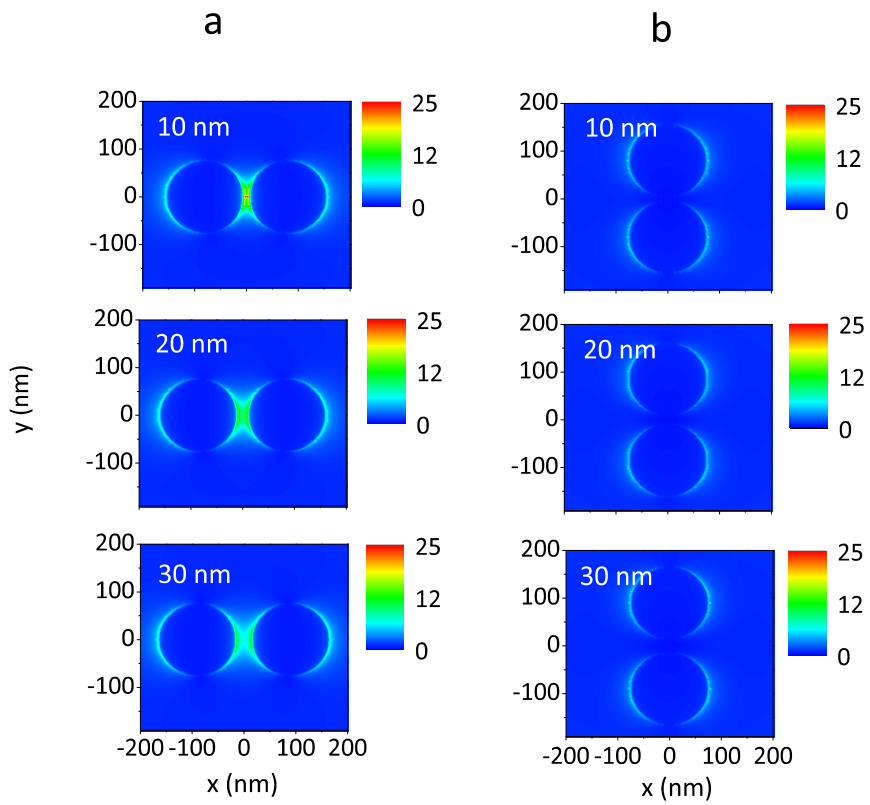

Figure 2.4. Near-field plots of longitudinal (a) and transverse (b) plasmon modes in Ni nanodimer particles with separations 10 nm, 20 nm and 30 nm, respectively, analytically calculated for the wavelength 800 nm. Image courtesy of Nicolò Maccaferri.

When individual plasmon modes interact, a low-energy (red-shifted) hybrid mode is obtained for in-phase oscillations with the incoming electric field of the charges of elementary nanoparticles whereas the out-of-phase oscillations represent the higher-energy mode that is blue-shifted. These in-phase and out-of-phase plasmon modes are also known as bonding and anti-bonding modes [23].

Multiple plasmon resonances occur for asymmetric particles such as pairs of metal nanoparticles, e.g. dimers, for different directions of light polarization. Depending on the direction of light polarization, *longitudinal* and *transverse* plasmon modes can be excited in a dimer particle (Fig. 2.4 and Fig. 2.5). For longitudinal light polarization the low-energy mode, or bonding mode, and the higher-energy mode, or antibonding mode, are accessible optically. At the same time, the anti-bonding mode for transversal light polarization is dark and can not be optically excited for a pair of identical nanodisks.

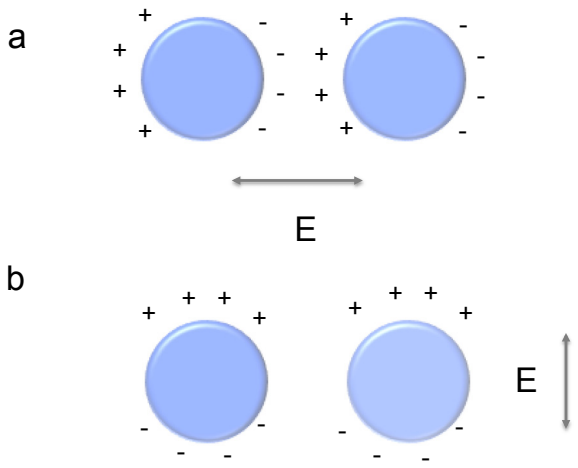

Figure 2.5. Illustration of electric dipole and plasma oscillations excited by localized plasmon resonance in a nanoparticle dimer for (a) bonding longitudinal and (b) optically accessible bonding transverse mode (following the definition given in [22]).

The restoring force, acting on the oscillating electrons is decreased due to Coulomb attraction between the opposite charges of neighboring particles for longitudinal light polarization when the bonding mode is excited (Fig. 2.5a), and increased due to Coulomb repulsion for transverse light polarization (Fig. 2.5b). Since the overall energy of the configuration is decreased, there is a red-shift of the plasmon resonance for the excitation of longitudinal mode. Oppositely, the increase in energy results in a blue-shift of the transverse mode [1, 18, 24]. Consequently, the longitudinal resonance redshifts as the interparticle distance get smaller (Fig. 2.6a) whereas the transverse resonance is much less sensitive to distance change between the particles (Fig. 2.6b).

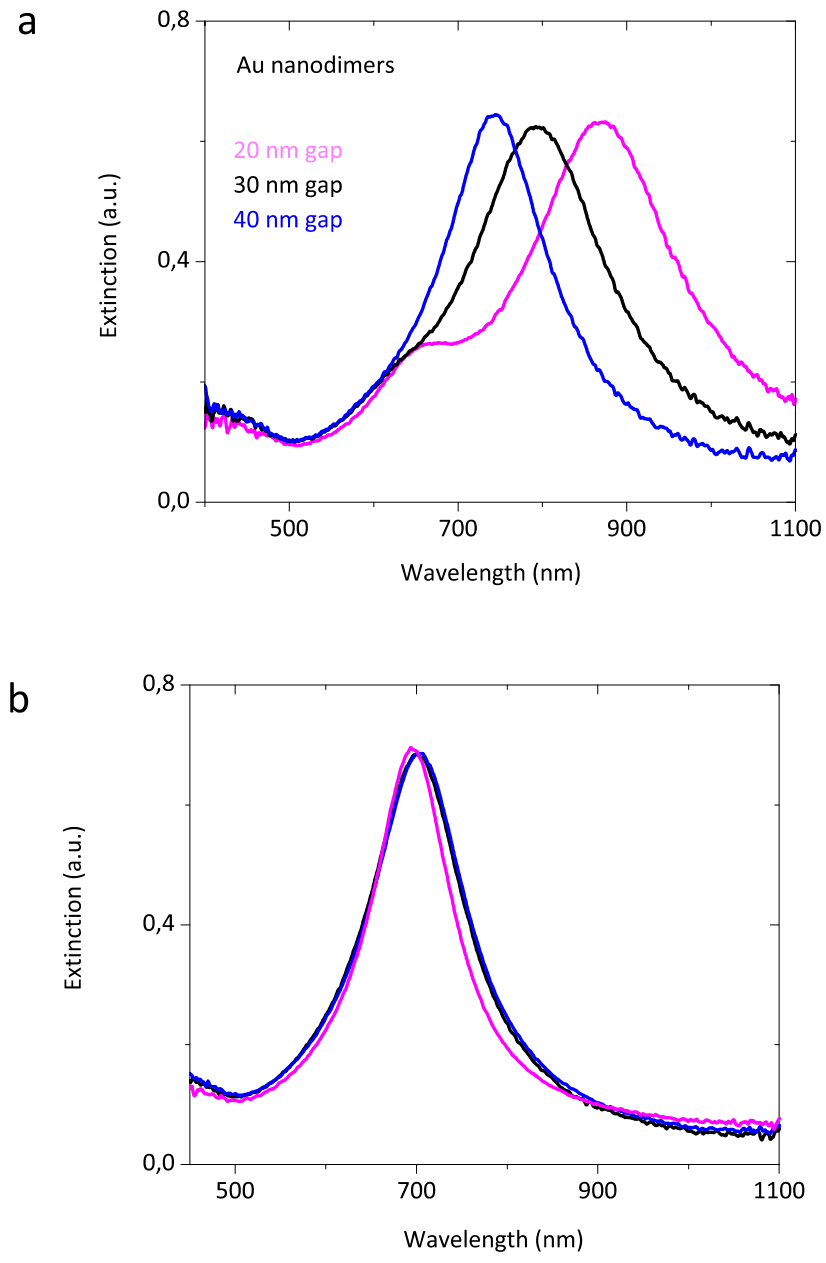

Figure 2.6. Longitudinal (a) and transverse (b) modes of localized plasmon resonances excited in Au nanodimers with interparticle separations 20 nm, 30 nm and 40 nm. The single disk diameter is 150 nm and the thickness is 30 nm.

Chapter 3

3 Magnetoplasmonics with nanoparticles

Chapter 3 is focusing on magneto-optics and magnetoplasmonics with nanoparticles. In section 3.1 I give a short introduction to magneto-optics and classification of different magneto-optical phenomena. Thereafter, I focus on the magneto-optical Kerr effect and provide the analytical description of optical properties of gyrotropic medium. In section 3.2 I describe the role of localized plasmons and spin-orbit coupling on magneto-optical activity, and derive the analytical expressions for the Kerr ellipticity and Kerr rotation. I close this chapter by explaining the fundamental property of localized plasmons to enhance and tailor the magneto-optical activity.

3.1 Introduction to magneto-optical effects

Magneto-optical effects appear when light interacts with matter subjected to a magnetic field. The origin of these effects is system energy splitting, known as Zeeman effect, which occurs in external magnetic field. The presence of a magnetic field is not necessary if a matter is magnetically ordered (ferromagnetic, ferrimagnetic, etc.), so magneto-optic effects appear in the absence of external magnetic field as well. In a magnetized matter, the magnetic field breaks the spatial and time-reversal symmetries leading to optical anisotropy, which manifests itself as dichroism, i.e. difference in the absorption coefficients for two orthogonal polarizations. Dichroism is defined as the difference between absorptions of the right-hand and left-hand circularly polarized components ($k_+ - k_-$) in the Faraday geometry (when $k \parallel H$), so-called *magnetic circular dichroism* (MCD). In Voigt geometry, when $k \perp H$, it is known as *magnetic linear dichroism* (MLD), or the difference between absorptions of components polarized parallel and perpendicular to the magnetic field. The splitting in dispersion curves of the absorption coefficient is related to the splitting in dispersion curves of the refractive index via Kramers-Kroning relations. It is observed as the difference between the refractive indices for the two circularly polarized components (also known as *magnetic circular birefringence* or *Faraday effect*) and for the two linearly polarized components (*magnetic linear birefringence*) in the Faraday and Voigt geometry, respectively [25].

The origin of dichroism and birefringence lies in symmetry breaking induced by a magnetic field. Magnetic field is an axial vector and has symmetry of circular current set out in a plane perpendicular to the vector of the magnetic field. Therefore, if a medium is placed in a magnetic field, the rotation directions in the plane perpendicular to the magnetic field are different. This means that in magnetized medium the optical properties for light propagating along the magnetic field direction with right-hand and left-hand circular polarizations are different too. The interesting analogy is symmetry breaking in a rotating medium along its rotational axis, which is explained by the fact that angular velocity, like magnetic field, is an axial vector [17, 25].

3.1.1 The Faraday effect

In 1845 Michael Faraday discovered that if a block of optical quality (heavy) glass, borosilicate of lead, is placed in a magnetic field, it becomes optically active [26]. When linearly polarized light passes through glass in a direction parallel to the applied magnetic field, the polarization plane is rotated by an angle Θ, which is proportional to the magnitude of the magnetic field H and the distance L, travelled by light:

$$\Theta = VHL. \tag{1}$$

The proportionality constant V, called the Verdet constant, is defined as the rotation per unit path, per unit field strength and depends on the material properties, photon energy and the temperature.

The Faraday effect originates from the difference in refractive indices of right-hand and left-hand circularly polarized components, $n_+ - n_-$, induced by the magnetic field. Linearly polarized light can be seen as a superposition of left- and right-hand circular waves with a defined phase difference. As a result of the difference between n_+ and n_-, the circular waves will propagate with different velocities c/n_- and c/n_+ when a magnetic field is applied, which causes the rotation of the polarization plane of the linearly polarized light by the angle [25]

$$\Theta = \frac{\omega}{2c}(n_+ - n_-)L, \tag{2}$$

where ω is angular frequency, c is the velocity of light and L is the path of the beam in

the medium. The phenomenological distinction of Faraday effect from natural optical activity (chirality) is non-reciprocity of the Faraday effect: the value of Θ will be doubled if light travels back along the same path through the magnetized medium (e.g. after reflection from a mirror). In case of natural optical activity, when light travels back after normal reflection, Θ = 0.

3.1.2 The magneto-optical Kerr effect (MOKE)

Along with magneto-optical effects arising during transmission of light through a magnetized medium, there are a number of effects, which manifest themselves when the light is reflected from a surface of a magnetized material. These phenomena are conventionally referred to as magneto-optical Kerr effects, discovered in 1877 by a Scottish physicist John Kerr, and can be classified to *longitudinal (meridional)*, *polar* and *transverse* (*equatorial*) Kerr effects according to the orientation of the magnetization vector relative to the reflective surface, or the plane of incidence of the incoming beam. Faraday and Kerr effects are *odd* effects, i.e. change sign when the sample is remagnetized [25].

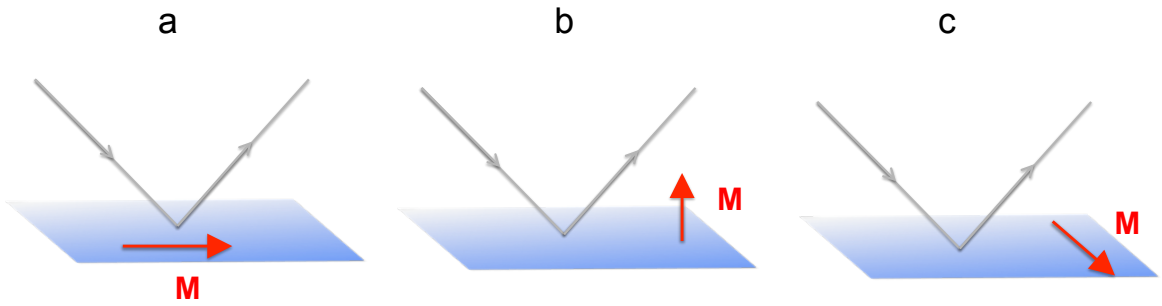

Figure 3.1. Geometry of the magneto-optical Kerr effect, showing the orientation of the vector of magnetization M with respect to the plane of light incidence in three configurations: (a) longitudinal, (b) polar and (c) transverse.

L-MOKE: In the longitudinal magneto-optical Kerr effect (L-MOKE) (Fig. 3.1a), the magnetization vector *M* lies both in the plane of the sample and in the plane of light incidence. In this effect, the polarization plane of the linearly polarized light is rotated and an ellipticity is introduced after the reflection from a magnetized surface (Fig. 3.2a).

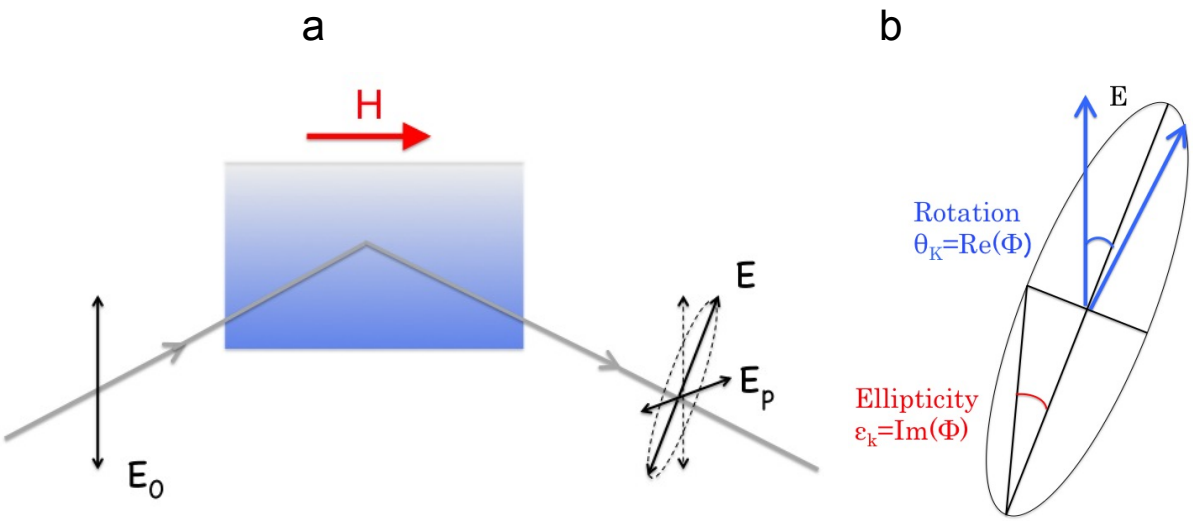

Figure 3.2. (a) Illustration of the rotation of the polarization plane and appearance of the elliptical component in L-MOKE. (b) Geometrical representation of the complex Kerr angle.

Kerr rotation and Kerr ellipticity compose the complex Kerr angle Φ_K (Fig. 3.2b) with Kerr rotation being its real part, $\Re[\Phi_K]$, and Kerr ellipticity being its imaginary part, $\Im[\Phi_K]$:

$$\Phi_K = \theta_K + i\epsilon_K. \tag{1}$$

Similar to the Faraday effect, L-MOKE is proportional to the magnetization and is primarily used to probe the magnetization of the sample being one of the most sensitive and simplest methods (Fig. 3.3). It is the main experimental technique used in this thesis to explore the magneto-plasmonic properties.

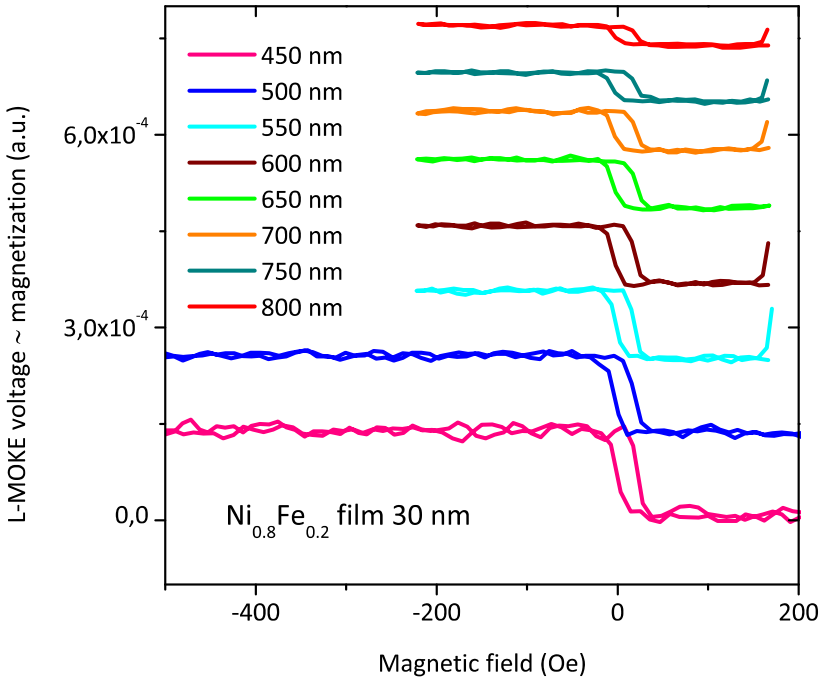

Figure 3.3. Magnetization hysteresis loops measured in permalloy ($Ni_{0.8}Fe_{0.2}$) film of the thickness 30 nm at wavelengths 450 nm, 500 nm, 550 nm, 600 nm, 650 nm, 700 nm, 750 nm and 800 nm by L-MOKE. The loops (apart from the one measured at 450 nm) are shifted from zero vertically for clarity of presentation and have the same scale.

P-MOKE: In the polar magneto-optical Kerr effect (P-MOKE), the magnetization vector *M* is oriented perpendicularly to the reflective surface and parallel to the plane of light incidence (Fig. 3.1b). Similarly to L-MOKE, this effect results in a rotation of the polarization plane and the appearance of ellipticity, though, giving values about one order of magnitude higher than L-MOKE. A common feature of the longitudinal and the polar MOKE is a presence of non-zero projection of the wave vector *k* on the magnetization plane. Polar Kerr effect is of great importance for optical data storage since it is used for reading the information from magneto-optical disks [25].

T-MOKE: In the transverse Kerr effect (T-MOKE), the magnetization vector is oriented perpendicularly to the plane of light incidence (Fig. 3.1c). It can only be observed for absorbing materials and results in intensity variation and phase shift of linearly polarized light reflected from a magnetized material. This effect is employed in observations of magnetic domains at the surface of a magnetized sample and in design of non-reciprocal optical devices, such as transversely magnetized mirrors [25].

3.1.3 Dielectric tensor of gyrotropic medium

The dielectric permittivity tensor of an isotropic material is given by:

$$\varepsilon = \begin{pmatrix} \varepsilon_{xx} & 0 & 0 \\ 0 & \varepsilon_{yy} & 0 \\ 0 & 0 & \varepsilon_{zz} \end{pmatrix}, \tag{1}$$

where the diagonal elements $\varepsilon_{xx} = \varepsilon_{yy} = \varepsilon_{zz} = \varepsilon$ and non-diagonal elements $\varepsilon_{ij} = 0, i \neq j$. In the medium which exhibits magneto-optical (MO) effects (gyrotropic medium), the dielectric tensor becomes non-diagonal [27]:

$$\varepsilon = \begin{pmatrix} \varepsilon_{xx} & \varepsilon_{xy} & \varepsilon_{xz} \\ \varepsilon_{yx} & \varepsilon_{yy} & \varepsilon_{yz} \\ \varepsilon_{zx} & \varepsilon_{zy} & \varepsilon_{zz} \end{pmatrix} = \begin{pmatrix} \varepsilon & -iQm_z & iQm_y \\ iQm_z & \varepsilon & -iQm_x \\ -iQm_y & iQm_x & \varepsilon \end{pmatrix}. \tag{2}$$

Here Q is the magneto-optical Voigt parameter and m_i is the magnetization in i-direction. The appearance of non-diagonal terms in the dielectric tensor is defined by the direction, in which the magnetic field is applied. If z is the direction of light propagation, xy is the sample plane, and the magnetic field or magnetization is aligned in z-direction (the case of P-MOKE), the dielectric tensor takes form:

$$\varepsilon_{P-MOKE} = \begin{pmatrix} \varepsilon & -iQm_z & 0 \\ iQm_z & \varepsilon & 0 \\ 0 & 0 & \varepsilon \end{pmatrix}. \tag{3}$$

Similarly, when the magnetic field is applied in x-direction (L-MOKE) and in y-direction (T-MOKE), the tensor is given by (4) and (5):

$$\varepsilon_{L-MOKE} = \begin{pmatrix} \varepsilon & 0 & 0 \\ 0 & \varepsilon & -iQm_x \\ 0 & iQm_x & \varepsilon \end{pmatrix}, \tag{4}$$

$$\varepsilon_{T-MOKE} = \begin{pmatrix} \varepsilon & 0 & iQm_y \\ 0 & \varepsilon & 0 \\ -iQm_y & 0 & \varepsilon \end{pmatrix}. \tag{5}$$

The presence of non-diagonal elements in the dielectric tensor means that the respective components of the electromagnetic field become coupled by the spin-orbit (SO)

interaction. MO is a result of SO interaction that couples transverse magnetic (TM or p) and transverse electric (TE or s) in a material and induces the change in the polarization state of the light. Specifically, when s-polarized (p-polarized) light reflects from the magnetized surface, it acquires a small p-polarized (s-polarized) component (Fig. 2a). The change in polarization state is described by non-diagonal Fresnel coefficients r_{ps} and r_{sp}, accounting for the polarization conversion, while the diagonal elements r_{pp} and r_{ss} are the reflection coefficients for p-polarized and s-polarized electromagnetic waves. One can express the complex Kerr angle, Kerr rotation θ_K and Kerr ellipticity ϵ_K, as follows:

$$\Phi_k = \theta_K + i\epsilon_K = \frac{r_{ps}}{r_{pp}}, \tag{6}$$

$$\theta_K = \Re\left(\frac{r_{ps}}{r_{pp}}\right), \tag{7}$$

$$\epsilon_K = \Im\left(\frac{r_{ps}}{r_{pp}}\right). \tag{8}$$

The non-diagonal Fresnel coefficients r_{ps} are responsible for polarization conversion and represent pure magneto-optical contribution to magneto-optical activity of the system, whereas the diagonal elements r_{pp} represent pure optical contribution to MO. Therefore, the overall MO response of the system may be enhanced by either increasing the MO contribution or reducing the optical contribution. An important property of localized surface plasmon resonance, namely strongly enhanced local fields, gives the enhancement in MO activity [28].

3.2 Effects of plasmons on magneto-optical activity

Localized plasmon resonances, due to the local field confinement at the nanoscale, result in greatly enhanced near-fields. Another consequence of strongly enhanced local electric fields is enhanced interaction with magnetic fields, leading to the enhancement of electromagnetic field in the material and, therefore, the MO activity. Despite the decreased volume of the active material, which is the consequence of nanostructuring, the Kerr rotation values become greatly enhanced due to the excitation of localized

surface plasmons, and may, like in Ni, at some wavelengths exceed the values measured for continuous films (Fig. 3.4).

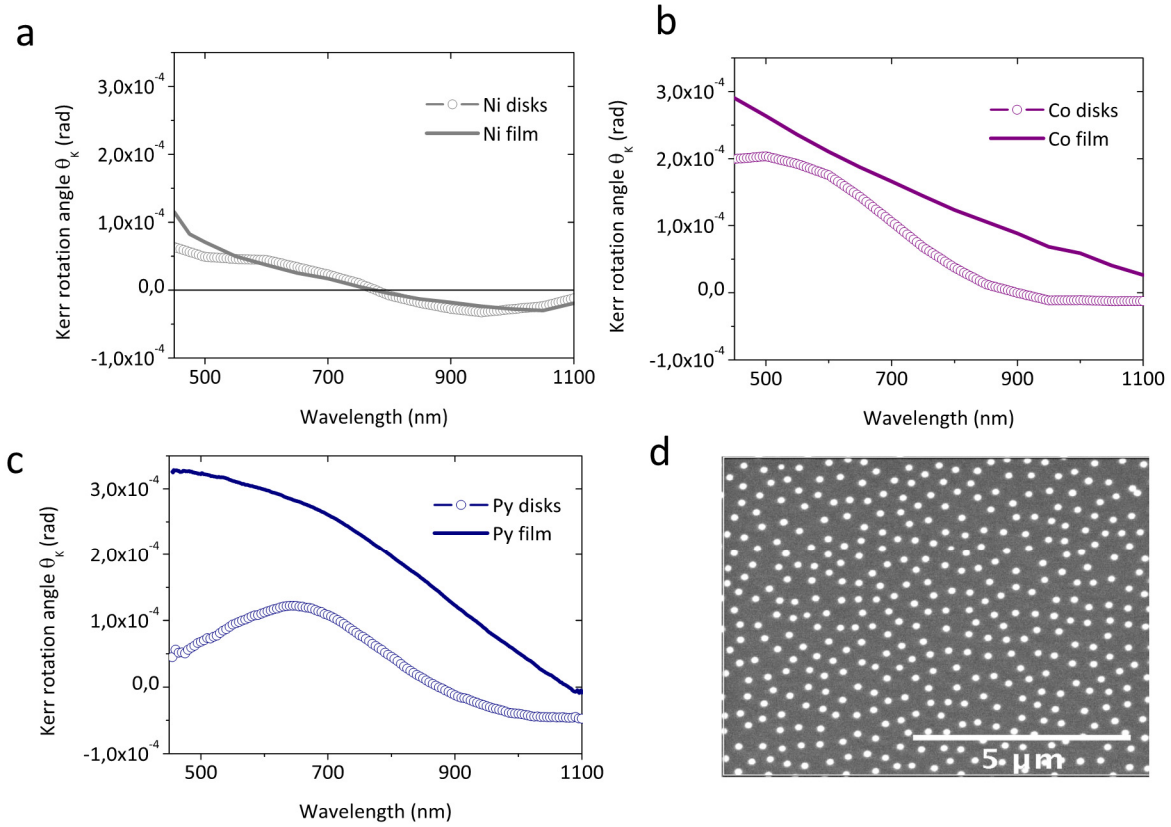

Figure 3.4. Kerr rotation values, measured for continuous films and nanodisks of the same thickness by L-MOKE. (a) Ni, (b) Co and (c) Permalloy ($Ni_{0.8}Fe_{0.2}$). (d) Scanning electron micrograph of permalloy nanodisks with diameter 170 nm and thickness 30 nm.

In addition to strong enhancement of the magneto-optical activity by plasmons, a broadband tunability can be achieved in magnetoplasmonic nanostructures. Localized plasmon resonances can be supported by purely ferromagnetic nanostructures; however, they exhibit a much stronger damping due to a large imaginary part of the dielectric constant [29]. It has been recently demonstrated that plasmon excitations in ferromagnetic nanoparticles induce the sign reversal of Kerr rotation and ellipticity [13], and allow the tuning of MO activity [12, 13], which, being an intrinsic property of matter, in principle, can not be freely manipulated. In noble metals the MO response is much weaker than in ferromagnetic materials and has to be accessed with very strong magnetic fields of several Tesla, compared to (0.5-1) Tesla in ferromagnetic materials. However, due to the huge near-fields induced by plasmon resonance excitation in noble metals, they can exhibit a sizable MO activity at low magnetic fields (of the order of 1 Tesla) [30, 31]. Unfortunately, localized plasmon resonances in ferromagnetic materials

are strongly damped and broadened due to high absorption and do not produce as high local fields as the noble metals (Fig. 3.5). A promising route in magnetoplasmonics is a design of hybrid nanostructures, combining a ferromagnetic and a noble material [11, 32], where the MO response can be boosted due to strong electromagnetic field enhancement. Moreover, by proper stacking the magnetic and plasmonic components it is possible to generate the MO activity in a non-magnetic element, with overall MO response exceeding the MO response of pure magnetic system [33-35] and significantly reduced optical losses[32].

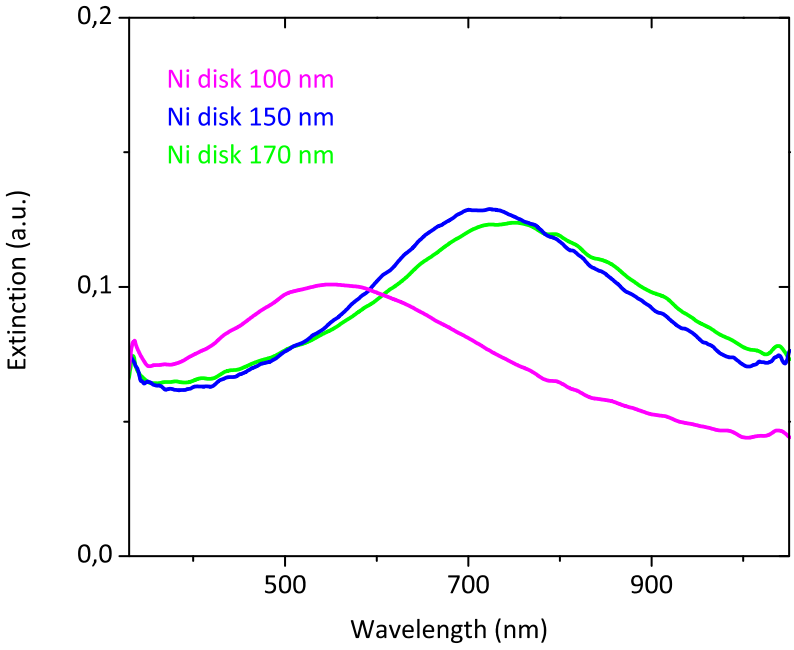

Figure 3.5. Localized plasmon resonances in Ni nanodisks with diameters 100 nm, 150 nm and 170 nm and thickness 30 nm.

3.2.1 Spin-orbit coupling effects on the magneto-optical activity

The interaction between plasmon resonances and MO activity can be understood from the derivation of polarizabilities of a single nanodisk, located in a magnetic field [36]. In L-MOKE geometry (Fig. 3.6a), the incident electric field E^0 along the y-axis induces an electric dipole along this axis, given by:

$$p_y = \alpha_{yy} E_y^o. \quad (1)$$

The electron oscillations along the y-axis are coupled thought the spin-orbit (SO) interaction with the magnetization M, which is oriented along the x-axis. This coupling

results in a dipole oscillation in the transverse direction along the z-axis. The expression for this dipole can be written in terms of non-diagonal elements of the polarizability tensor, as [36]:

$$p_z = \alpha_{zy} E_y^o. \tag{2}$$

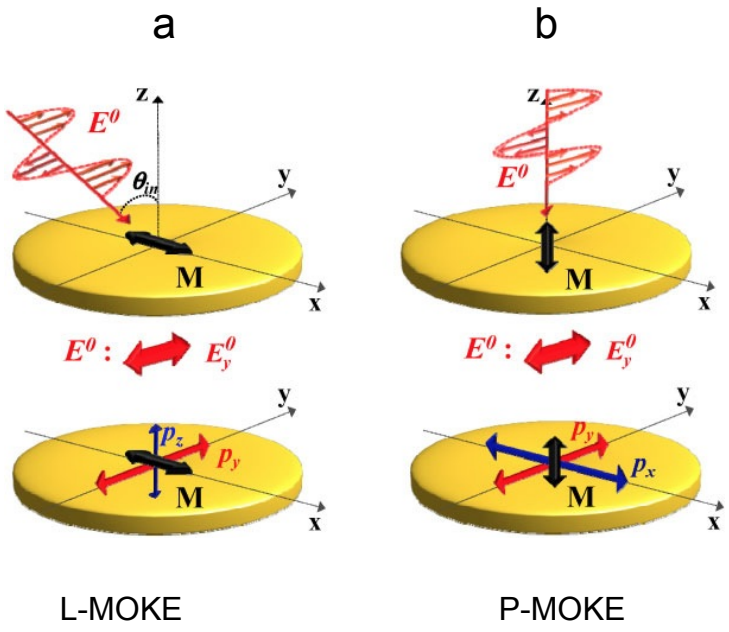

Figure 3.6. Longitudinal (a) and polar (b) MOKE configurations for an isolated nanodisk with xz being the scattering plane. In L-MOKE (left), the incident electric field E_y^o induces a direct dipole p_y, which generates a dipole p_z through the spin-orbit coupling. In P-MOKE (right), the incident electric field E_y^o is exciting p_y and spin –orbit induced dipole p_z. The figure is adapted from [36].

As it is explicitly shown in [36], the general expression for the non-diagonal elements of the polarizability tensor is given by:

$$\alpha_{kj} = \frac{\varepsilon_{kj}\alpha_{kk}\alpha_{jj}}{(\varepsilon - \varepsilon_m)^2}, \tag{3}$$

with ε_m being the dielectric permittivity of the surrounding medium and ε_k, the non-diagonal elements of the dielectric tensor

$$\varepsilon = \begin{pmatrix} \varepsilon_{xx} & \varepsilon_{xy} & \varepsilon_{xz} \\ \varepsilon_{yx} & \varepsilon_{yy} & \varepsilon_{yz} \\ \varepsilon_{zx} & \varepsilon_{zy} & \varepsilon_{zz} \end{pmatrix}. \tag{4}$$

The diagonal elements of polarizability tensor α_{ii} of a single nanodisks are defined by the expression [37]:

$$\alpha_{ii} = \frac{\varepsilon_m(\varepsilon - \varepsilon_m)}{\varepsilon_m + N_{ii}(\varepsilon - \varepsilon_m)}, \tag{5}$$

were N_{ii} is depolarizing factor along i-direction.
By setting $k = z$ and $j = y$ in formula (2), the expression for the electric dipole, induced by SO coupling is obtained as follows:

$$p_z = \alpha_{zy} E_y^o = \left[\frac{\varepsilon_{zy}\alpha_{yy}\alpha_{zz}}{(\varepsilon - \varepsilon_m)^2}\right] E_y^o. \tag{6}$$

In P-MOKE geometry illustrated in Fig. 3.6b, the electric field E_y^o at normal incidence induces an electric dipole $p_y = \alpha_{yy} E_y^o$, which now is coupled through SO coupling with magnetization M in x-direction. This coupling results in a transverse dipole along x-axis, according to (3):

$$p_x = \alpha_{xy} E_y^o = \left[\frac{\varepsilon_{xy}\alpha_{xx}\alpha_{yy}}{(\varepsilon - \varepsilon_m)^2}\right] E_y^o. \tag{7}$$

The MO activity is totally determined by the transverse localized plasmon resonances induced by the spin-orbit coupling and is not influenced by the plasmon resonances excited by direct illumination. It will be shown in the next section.

3.2.2 Tailoring the magneto-optical activity with plasmons

In analogy with formula (6) in 3.1.3 and using the expressions for p_y and p_z in 3.2.1, the complex Kerr angle in L-MOKE configuration (as it is presented in Fig. 3.6a in previous section 3.2.1) can be extracted:

$$\Phi_k{}^L = \frac{p_z}{p_y} = \frac{\varepsilon_{zy}\alpha_{yy}\alpha_{zz}\sin\theta_{inc}}{(\varepsilon - \varepsilon_m)^2\alpha_{yy}}, \tag{1}$$

where $\sin\theta_{inc}$ accounts for the angular dependence of spin-orbit induced dipole p_z, when θ_{inc} is the incidence angle of the incoming electric field. Similarly, the expression for the complex Kerr angle in P-MOKE configuration is presented by:

$$\Phi_k{}^P = \frac{p_x}{p_y} = \frac{\varepsilon_{xy}\alpha_{yy}\alpha_{xx}}{(\varepsilon - \varepsilon_m)^2\alpha_{yy}}. \quad (2)$$

As we can notice, the terms α_{yy} related to the polarizabilities of directly excited dipole in the expression (1) and (2) cancel out. The fundamental consequence of these equations is that plasmon-induced enhancement and phase tuning of MO response occur due to the transverse resonance excited due to the SO coupling. From these expressions it follows that the non-diagonal terms in permittivity tensor are the key elements in broadband tunability of both Kerr rotation and Kerr ellipticity, composing the complex Kerr angle. This fundamental property motivates the engineering of complex 2D and 3D nanostructures where several spectrally separated plasmon resonances allow the broadband control of MO activity and the polarizabilities can be tailored at will [38]. As it is explicitly demonstrated in [12] and [38], controlling the shape and the size of magnetoplasmonic nanostructures opens up a possibility to tailor the polarization state of the reflected light and obtain hugely enhanced values of the Kerr rotation.

Chapter 4

4 Introduction to plasmon nanorulers

Accurate measurements of distances on the nanoscale are decisive in many aspects of the materials and life sciences. Prominent examples include studies of various biochemical processes via conformational changes in biomolecules. Previously, the optical tools used to obtain spatial information on the nanoscale, and down to the single-molecule level, focused on Förster resonance energy transfer (FRET) spectroscopy and the use of organic fluorophoresin in so-called molecular rulers. Dynamic processes, such as DNA bending and cleavage, and RNA catalysis and folding, as well as protein–protein interactions, were all first explored by FRET. However, the limitation of fluorophores due to their photo bleaching and degradation over time led to the emergence of noble-metal nanoparticle-based plasmon rulers [39-42]. The operation of plasmon rulers relies on localized collective electronic oscillations (localized plasmons) in nanometal assemblies and on the near-field coupling (i.e., hybridization) between the plasmon modes of the adjacent nanoparticles, which strongly depends on the interparticle distance [22, 43]. Plasmon local electromagnetic near-fields exponentially decay over distance and as such, at small separations, the near-field enhancement and coupling effects increase dramatically. The underlying idea of a plasmon ruler, which consists of two or more noble metals or elements of core–shell structures, is then the extreme sensitivity of the light scattering to the interparticle gap size [22, 23, 43-48]. This was first explored with nanoplasmonic dimer antennas almost a decade ago for monitoring the kinetics of single DNA hybridization events in solution (see Fig. 4.1 that also explains the working principle of a plasmon ruler) [39].

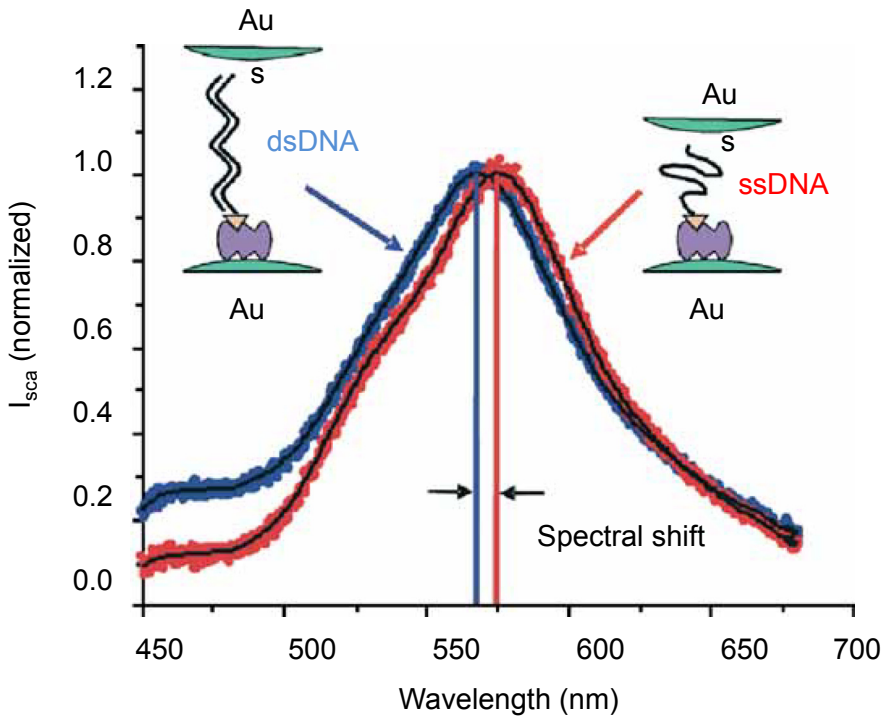

Figure 4.1. Example of a spectral shift between a gold particle pair connected with ssDNA (red) and dsDNA (blue). The shift is clearly visible. The figure is taken from [39].

In later realizations, plasmon rulers with sub-nm resolution consisted of thin-film coupled single-particle nanoantennas that utilized thiol monolayers with an adjustable chain length [40]. The principles of plasmon ruler design are typically refined with lithographically fabricated nanoantennas that are implemented to investigate the distance dependence of plasmon-coupling effects and to derive a plasmon ruler equation [41]. This includes the concept of a multielement three-dimensional plasmon ruler [42] to track the complex conformational changes that have also been recently realized in solution [49].

Chapter 5

5 Experimental methodology

5.1 Nanofabrication of plasmonic and magnetoplasmonic nanorulers

Hole–mask colloidal lithography (HCL) is a bottom-up nanofabrication method utilizing the self-assembly of negatively charged sulfate latex microspheres. We used microscope slide glass (VWR International) of dimensions 10 mm × 10 mm × 1 mm as a substrate. The substrate was cleaned by ultrasonication in acetone and exposed to reactive ion etching (RIE) by oxygen O_2 plasma (5 s, 50 W, 250 mTorr, Plasma ThermBatchTop PE/RIE m/95) in order to increase polymer adhesion to the glass. The layer of polymethyl methacrylate (950PMMA 4% diluted in anisole, MW = 950000, MicroChem), 235 nm thick, was spin-coated on the substrate and baked at 180 °C in a convection oven for 10 min. After baking, O_2 plasma was applied for 5 s to make the PMMA hydrophilic. In the next step, the substrate with the PMMA layer residing on it was functionalized with polydiallyldimethylammonium chloride (PDDA, MW = 200000–350000, 0.2% solution in deionized (DI) water), rinsed with DI water and dried using an N_2 gun. Negatively charged polystyrene beads (sulfate latex beads, 0.2% suspended in DI water, Invitrogen) were pipetted onto the substrate and kept there for 120 s. After careful rinsing with DI water, the substrate was immediately dried with the N_2 gun at normal flow incidence to avoid bead removal or aggregation. Further evaporation of a very thin Au layer followed by tape-stripping of the spheres (SWT-10 tape, Nitto Scandinavia AB) and reactive ion etching (RIE) by O_2 plasma through the entire thickness of the PMAA layer created an evaporation mask, which can be employed in the fabrication of a variety of nanostructures [50]. In case of nanoparticle dimers, O_2 plasma etching is applied longer, such that a sufficient undercut in the PMMA is obtained, facilitated by the anisotropic nature of dry etching. This undercut is crucial for angular evaporation, which is used to fabricate a nanoparticle dimer. The samples were tilted during the main material evaporation, and then rotated by 180 degree to produce a binary nanoparticle. The tilt and rotation were repeated 3 times with small increments in thickness (10 nm) to minimize the difference in particle size. Finally, lift-off of PMMA completed the

fabrication procedure. The gap between the particles is tuned by varying the evaporation angle.

HCL method combined with angular electron beam evaporation allows producing nanoparticle dimers with nicely controlled nanogap size. The micrographs of the nanorulers with several nanogap sizes are provided in Fig.5.1. The limitation of HCL in producing dimer rulers with exceedingly large nanogaps (i.e., at 50 nm and above) stems from the fact that the model nanofabricated rulers in our case can only be separated by the distance roughly twice the nanodisk diameter in the ruler. That is, at 50 nm nanogap the inter-ruler distance becomes smaller than the nanogap itself. Though plasmonically these effects are not extremely pronounced (see Fig. 6.13 in Section 6.7 of Chapter 6 with nanogaps up to 60 nm), magneto-optically and magnetoplasmonically the Kerr polarization rotation measurements with such ruler become progressively poor-defined.

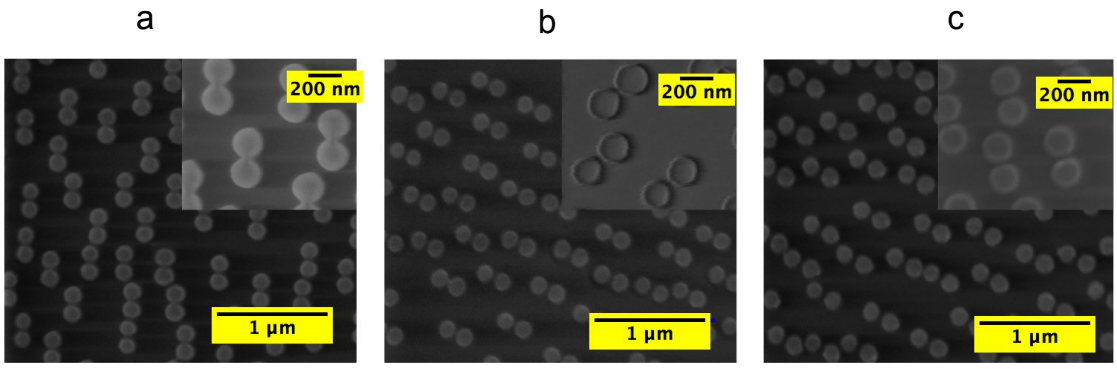

Figure 5.1. Scanning electron micrographs of magnetoplasmonic nanorulers with (a) 10 nm nanogap, (b) 20 nm nanogap and (c) 30 nm nanogap fabricated with HCL.

5. 2 Spectroscopic L-MOKE technique

A full description of Kerr effect requires measurement of both rotation θ_K and ellipticity ϵ_K. The experimental set-up used in this thesis is based on the polarization-modulation technique [51] and includes a photo-elastic modulator (PEM). The spectroscopic magneto-optic response of the magnetoplasmonic nanorulers is measured with a home-built L-MOKE set-up at an angle of light incidence of 25°, sketched in Figure 5.2.

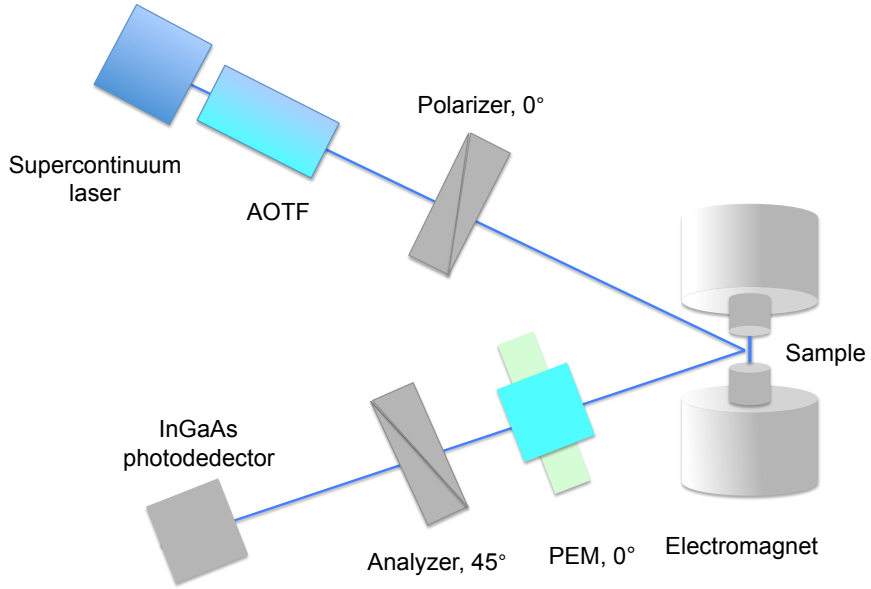

Figure 5.2. Schematic representation of spectroscopic L-MOKE set-up, where a straight line shows the light path.

The light is generated by ultra-broadband supercontinuum laser source (Fianium, Ltd.), which can potentially emit a radiation in the wavelength range from 450 nm to 2000 nm with a maximum power output about 5W. The output from the laser is connected to dual acousto-optic tunable filter (AOTF), which is used to filter-out a particular wavelength. AOTF consists of two piezoelectric crystals, designed to work in two optical regions: the visible range 450 nm- 600 nm and visible- near-infrared range 600 nm-1100 nm. A monochromatic laser beam from AOTF is sent through a multimode optical fiber with a collimating lens. This laser beam passes a rotatable Glan-Thompson polarizer (Newport), which can be set to provide either p-polarized or s-polarized light. The sample is placed between in a gap of the ferrite electromagnet so that the magnetization is induced in the sample plane and parallel to the plane of light incidence. The magnetic field of 2500 kOe of both polarities is applied in order to ensure the complete magnetization saturation of the samples. When linearly polarized laser beam reflects from a magnetized sample surface, the rotation θ_K and ellipticity ϵ_K are introduced. The reflected beam passes through a photo-elastic modulator (PEM-90, Hinds instruments) which provides a polarization modulation at frequency $\omega = 50\ kHz$. After passing a second Glan-Thompson polarizer, or analyzer, set to 45°, the light is detected by InGaAs avalanche photodetector (Thorlabs). The signal from the photodetector is sent to two lock-in amplifiers (Standford Research Systems, SR830DSP), which measure the components of the signal modulated at the ω and 2ω [51]. The DC component of the signal is measured by highly sensitive digital multimeter (Keithley, 2400).

The analytical description of the operation of L-MOKE technique is presented below. The intensity of light arriving at the photodetector may be written as [52]:

$$I(t) = I_0(1 + 2\theta_k \cos(A_0 \omega t) - 2\epsilon_k \sin(A_0 \omega t)), \quad (1)$$

where I_0 represents the DC intensity, $\omega = 2\pi f$ is the angular frequency of PEM oscillations, A_0 is the retardation amplitude of the PEM, θ_K is Kerr rotation and ϵ_K is Kerr ellipticity. Using a Fourier series expansion and keeping only the first three terms gives:

$$I(t) \cong I_0(1 + 2\theta_k J_o(A_o) - 4\epsilon_k J_1(A_0) \sin(\omega t) + 4\theta_k J_2(A_0) \cos(2\omega t)), \quad (2)$$

with J being Bessel functions. Here the first two terms are the parts of DC signal, when the second term can be neglected if the retardation A_o is set to 2.405 radians, in which case J_o=0. There are three voltages measured in the L-MOKE experiment: V_{DC}, V_{1f} and V_{2f}. It is convenient to express Kerr rotation θ_K and Kerr ellipticity ϵ_K as a ratio of the AC term to the DC term in order to avoid the influence of fluctuations in the light intensity during the experiment. The final expressions are, therefore, given by:

$$\theta_k = \frac{\sqrt{2}}{4J_2} \frac{V_{2f}}{V_{DC}} \quad (3)$$

$$\epsilon_k = \frac{\sqrt{2}}{4J_1} \frac{V_{1f}}{V_{DC}} \quad (4)$$

Chapter 6

6 Active magnetoplasmonic nanorulers

In this Chapter we present a new concept of active magnetoplasmonic ruler. It consists of magnetoplasmonic dimer antennas and is capable of reporting nanoscale distances via spectrally-resolved longitudinal magneto-optical Kerr effect (L-MOKE) while optimizing its own orientation. The externally applied magnetic field in MOKE potentially allows the *active* operation when the ruler can be aligned parallel to the magnetic field. We demonstrate that the best sensitivity and figure-of-merit are achieved when the ruler is oriented parallel with its longitudinal (magnetically easy) axis to both electric and magnetic fields.

6.1 Optical characterization

We first probe the magnetoplasmonic ruler with conventional optical (extinction) spectroscopy. We use two archetypical magnetoplasmonic materials, Ni [12, 13, 36-38] and Co [35, 53], to fabricate large-scale short-range-ordered bottom-up arrays of nominally identically oriented nanodisk (with diameter 150 nm and height 30 nm) dimers with nanogap sizes 10 nm, 20 nm, 30 nm, 40 nm and 50 nm by means of hole–mask colloidal lithography (see Section 5.1 of Chapter 5 for details) [50] (Fig. 6.1a, only rulers with nanogap sizes 10 nm, 20 nm and 30 nm are shown). Optical extinction spectra display highly damped plasmon resonances in both Ni and Co rulers, which, when hybridized, have rather broad spectral features both along the longitudinal (Figures 6.1b, c, left panels) and transversal (Figures 6.1b, c, right panels) axes of the ruler. The broad resonance shape prevents the strongly pronounced modification of the spectral optical response with varying gap size, as opposed to conventional plasmon rulers. For Ni rulers, we observe reasonably visible red shifts of the longitudinal hybrid plasmon resonance with decreasing gap size and a hint of a blue shift of the tangential resonance with decreasing gap size (Figure 6.1b). In Co rulers, the same features in both resonances become even less evident due to the increased dielectric losses in the material (Figure 6.1c).

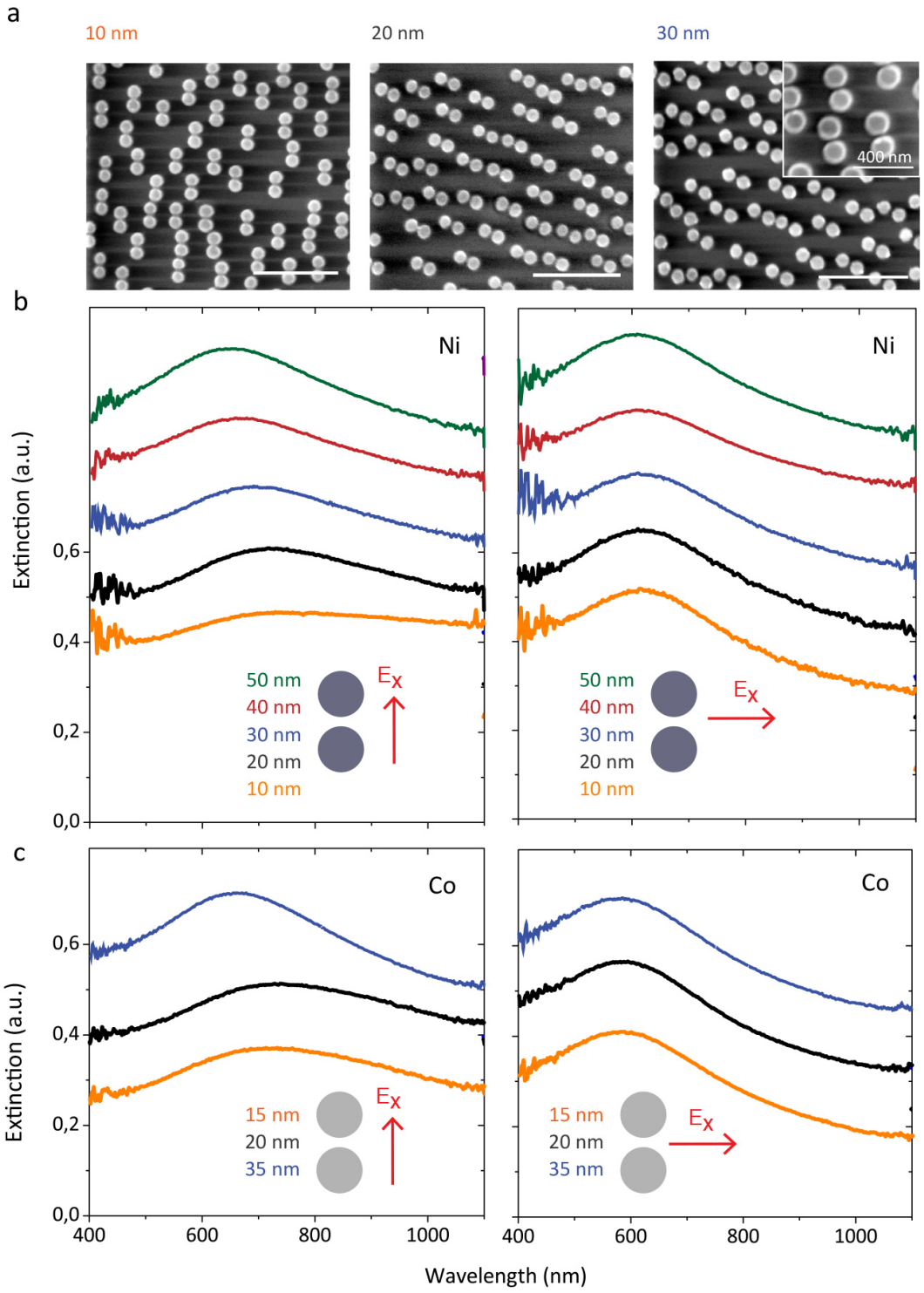

Figure 6.1. (a) Scanning electron microscopy (SEM) images of Ni magnetoplasmonic rulers with gap sizes of 10 nm (left), 20 nm (center), and 30 nm (right). Scale bars: 1µm. (b) Extinction spectra of Ni rulers and (c) extinction spectra of Co rulers for orientations of the electric field along (left) and perpendicular to (right) the longitudinal ruler axis. Data shifted vertically for clarity of presentation.

6.2 Analytical calculations of near-field and far-field response

We map the near-field and far-field optical responses of magnetoplasmonic rulers with a simple dipole–dipole model and finite-difference time-domain (FDTD) simulations (Figure 6.2). The dimensionless polarizability tensor of a single disk is given by

$$\tilde{\alpha} = \frac{Vk^3}{4\pi} \frac{\tilde{\varepsilon} - \tilde{I}}{\tilde{I} + \tilde{N}(\tilde{\varepsilon} - \tilde{I})} \tag{1}$$

where V is the volume of the ellipsoid $4\pi r_1^2 r_2/3$ (r_1 is the in-plane radius and r_2 is half-thickness of the disk); $\tilde{\varepsilon}$ is the dielectric tensor of Ni, $\tilde{I}$ is the identity matrix, and $\tilde{N}$ is the depolarizing tensor accounting for the shape and size of the particle and related radiative losses. Illuminating the dimer ruler along the longitudinal axis promotes the emergence of the so-called bonding mode in the visible spectral range, generating a reasonably strong near-field coupling between the elements, which then results in a pronounced dependence of the optical response on the gap size (Fig. 6.2a: see both far-field extinction cross-sections and near-field plots for various gap distances).

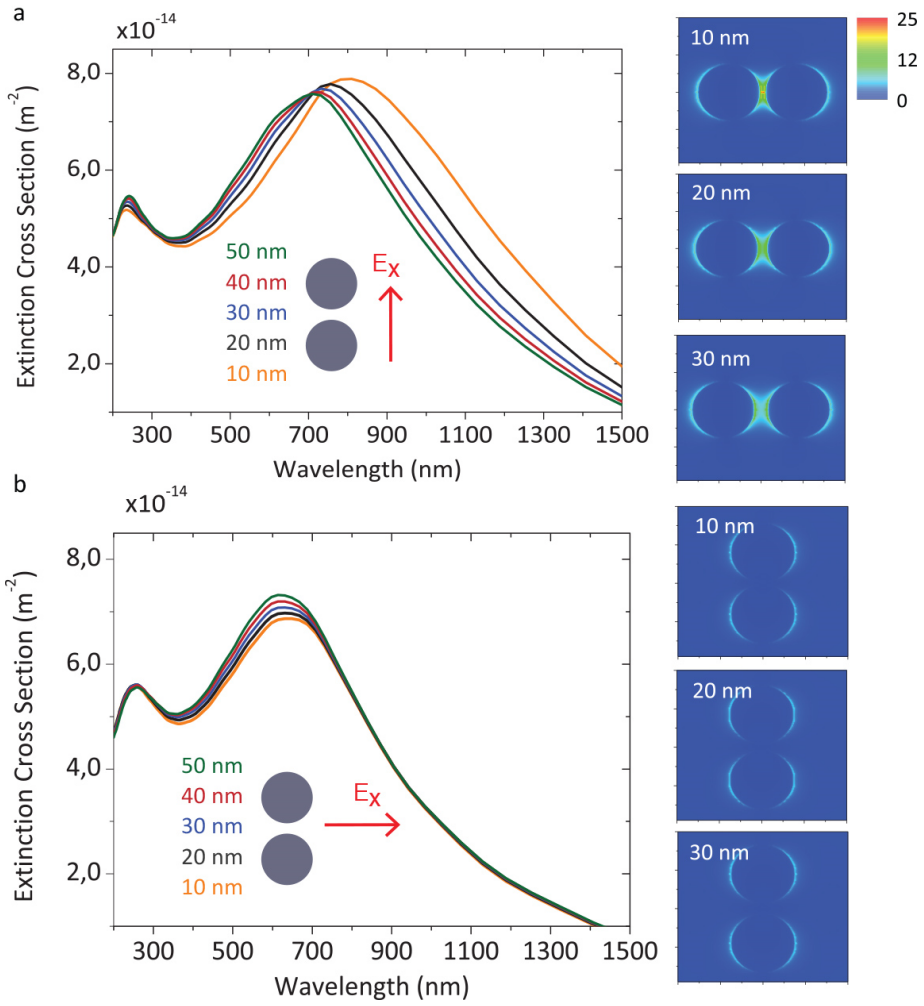

Figure 6.2. FDTD calculated far-field extinction spectra (left) and near-field response (right) for longitudinal (a) and transversal (b) plasmon modes of Ni magnetoplasmonic rulers with various nanogaps.

Specifically, rapidly decreasing the near-field coupling between the ruler elements while increasing the gap distance (Fig. 6.2a, near-field plots on the right panel) produces a sizeable blue shift in the optical extinction (Fig. 6.2a, left panel). The antibonding mode then falls into the UV region (see the feature in calculated extinction cross-section below 300 nm in Fig. 6.2a) and produces a near-field redistribution from the gap (Figure 6.3).

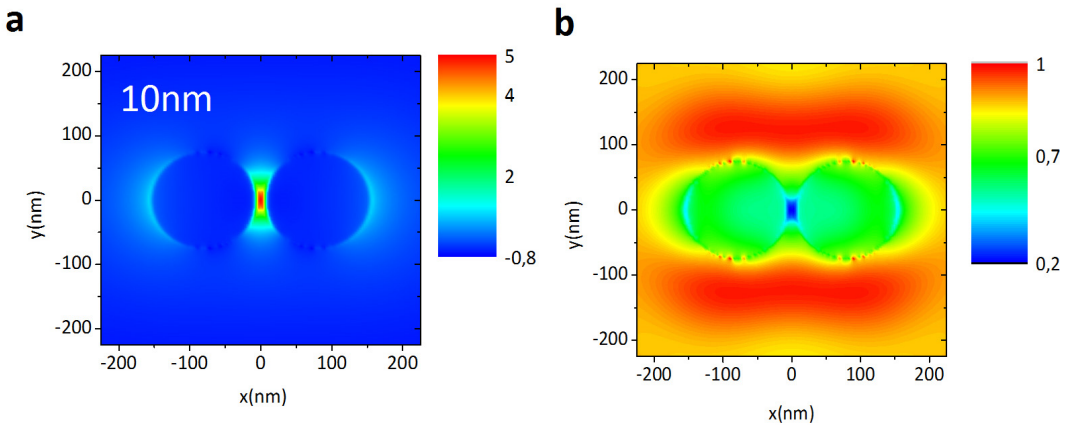

Figure 6.3. Near-field plots of longitudinal bonding (a) and antibonding (b) modes for 10 nm nanogap Ni ruler, calculated at wavelengths 800 nm and 240 nm respectively.

The coupling induced by linearly polarized light along the transversal axis of the ruler is far less pronounced, and the optical response correlates very weakly with the changing gap in the ruler (Fig. 6.2b, left panel for far-field optical extinction, right panel for near-field maps), similarly to the experimental observations (Fig. 6.1b). Overall, from a purely optical point of view, the magnetoplasmonic ruler behaves in accordance with the results of previous theoretical and experimental studies on noble-metal-based plasmon rulers [22, 39-48].

6.3 Figure-of-merit of plasmon rulers

To quantify the performance of a plasmon ruler in reliably measuring nanogaps, we introduce a figure-of-merit (FOM), defined as the ratio between sensitivity and the width of the resonance peak—a concept that is widely used to evaluate the performance of nanoplasmonic (bio)sensors by directly correlating the biodetection sensitivity and the resolution [54]. We take two previously reported plasmon rulers as examples—the dimer nanoantenna [47] and the particle-on-the-film [40]—to extract the FOM from the reported spectroscopic data in the 30–10 nm gap regime and obtain a FOM of 0.325 and 0.316, respectively. In addition, we fabricate Au dimer nanorulers with 150 nm nanodisks and separations of 20 nm, 30 nm and 40 nm by HCL, which produce FOMs of 0.39 and 0.31 going from 20 nm to 30 nm and 30 nm to 40 nm gaps, respectively, which is in line with extracted FOMs of previously reported ruler systems. We also model the phase of Au dimer nanorulers (Fig. 6.4) and obtain slightly higher phase-based FOMs of 0.62 and 0.37 for the regimes mentioned above. We do this since following the phase

rather than the amplitude of the localized plasmon resonances typically gives higher FOMs in plasmonic (bio)sensing. This is indeed the case as well for the plasmon rulers.

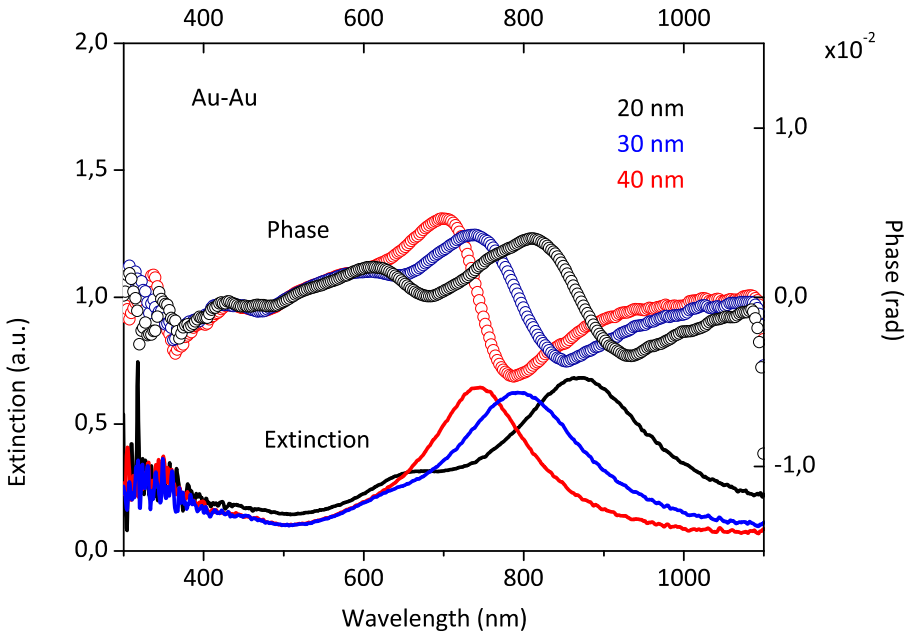

Figure 6.4. Experimental optical extinction spectra and extracted respective phases of the longitudinal bonding mode in Au nanorulers with gap separations 20nm, 30 nm and 40 nm.

6.4 Magnetic characterization

From a purely magnetic standpoint, the dimers display the well-known hysteretic behavior, typically observed in anisotropic ferromagnetic nanostructures. More specifically, the hysteresis magnetization loops, measured by alternating gradient magnetometry (AGM) (see Figure 6.5), show the expected easy (high remanence and coercivity) and the hard (relatively low remanence and coercivity) magnetization axes.

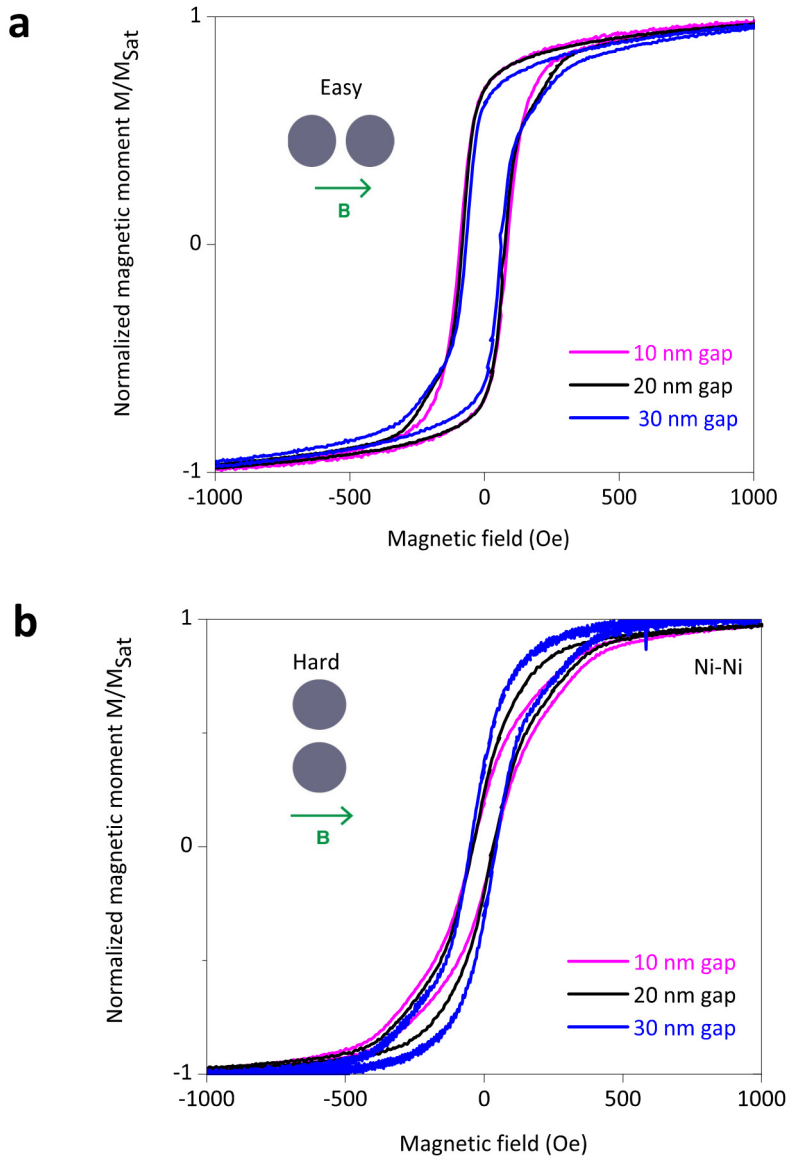

Figure 6.5. Hysteresis loops of Ni nanodimer rulers with 10 nm, 20 nm, and 30 nm gaps measured using Alternating Gradient Magnetometry (AGM).

6.5 Magneto-optical characterization with L-MOKE spectroscopy

As the next step, we demonstrate the superior operation of the magnetoplasmonic ruler, which proves to be almost two orders of magnitude better in terms of the FOM than the plasmonic rulers. We probe the magnetoplasmonic ruler using longitudinal MOKE (L-MOKE) spectroscopy [51]. Figure 6.6 shows the schematics of the

measurement geometries used for this purpose. For each of the polarization states (*p* and *s*; Figs. 6.6a, b and c, d, respectively) in L-MOKE, there are two available orientations of the electric field of light and the externally applied magnetic field with respect to the ruler axes. We denote these *p*-long, *p*-short, *s*-long, and *s*-short, depending on the orientation of the electric field of light with respect to the ruler, or dimer, axis (long or short). Specifically, for *p*-polarized light, the electric field and the magnetic field are parallel (Figure 6.6a, b); while for *s*-polarized light, they are orthogonal to each other (Figure 6.6 c, d). For *p*-polarized light, when the ruler is illuminated at 25° from the plane of incidence of the light (the plane marked in orange in all panels of Fig. 6.6), the $\vec{E}_{inc}$ has two components $\vec{E}_x$ (along the ruler's longitudinal axis) and $\vec{E}_z$. The latter, though applied to optically non-resonant mode, can efficiently couple to the magnetic field via the magneto-optical (MO) activity and induce a resonant MO dipole along the *y*-direction. For *s*-polarized light, only one component of the electric field $\vec{E}_y$ is available (Figs 6.6c, d); this couples to the off-resonant MO dipole induced along *z*, not related to the ruler gap [12, 38].

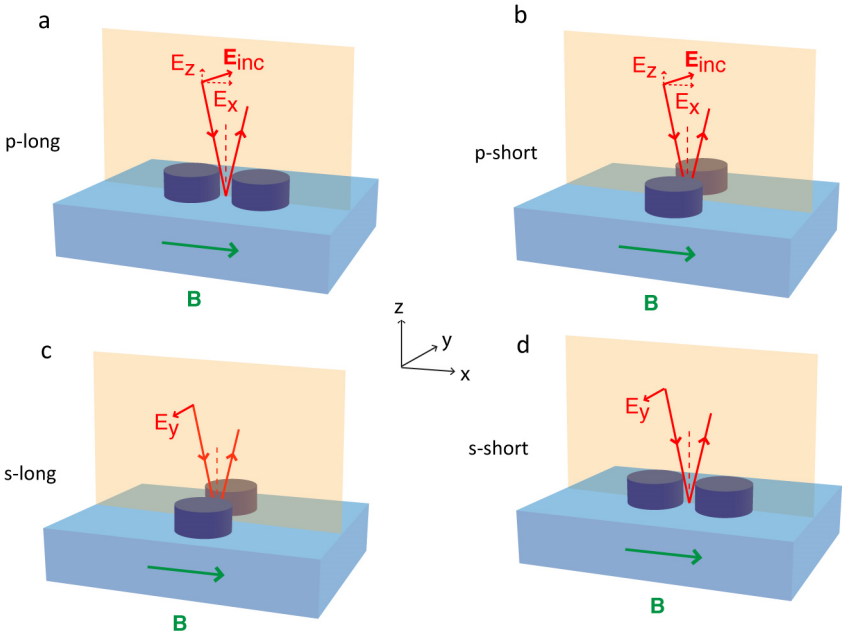

Figure 6.6. Schematics of the L-MOKE measurements for *p*-polarization (a and b) with the electric field along the long (a) and short (b) ruler axes and *s*-polarization (c and d) with electric field along the long (c) and short (d) ruler axes. The magnetic field is always along the *x*-axis.

We summarize the Kerr polarization rotation produced by Ni magnetoplasmonic rulers in Figure 6.7. Here, the differences due to the nanogap size become very pronounced, especially with *p*-polarized light (Figs. 6.7 a, b). It can easily be seen how the Kerr

rotation spectra blue shift when the nanogap is progressively reduced from 50 to 10 nm, when both magnetic field and $\vec{E}_x$ are parallel to the longitudinal ruler axis (Fig. 6.7a, *p*-long). In the *p*-short configuration (where both magnetic field and $\vec{E}_x$ are along the tangential ruler axis), a slight red shift occurs as the nanoscale distance in the ruler decreases. Similar shifts of the Kerr rotation spectra are detected with Co magnetoplasmonic rulers (Fig. 6.8).

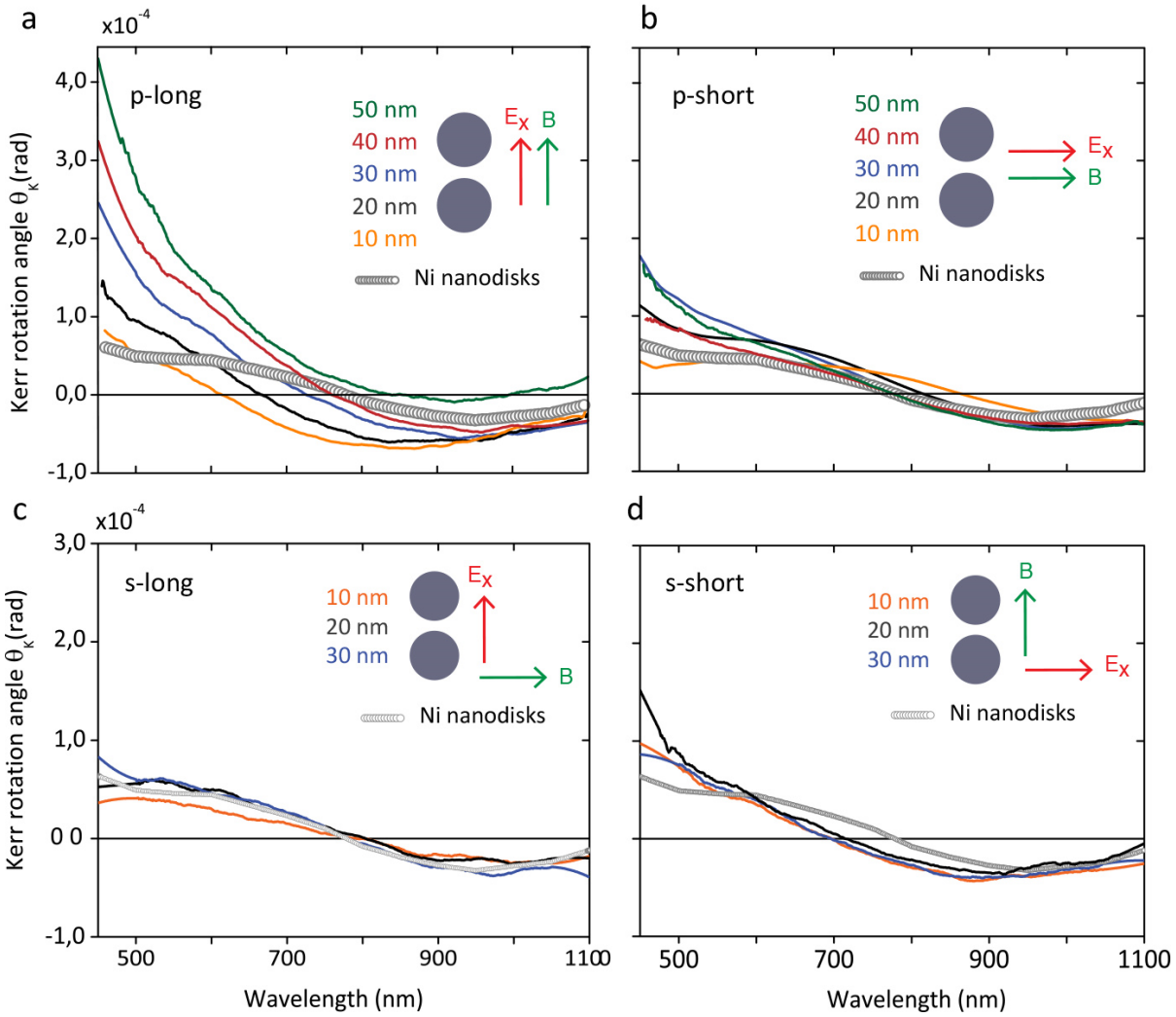

Figure 6.7. Spectral Kerr polarization rotation in Ni rulers with various nanogaps, along with Ni nanodisks antennas for the L-MOKE configurations described in Figure 6.6.

In stark contrast with the *p*-configurations, the magnetoplasmonic ruler essentially does not show any sensitivity to the nanogapsize with the *s*-polarized illumination, as the Kerr polarization rotation spectra become largely indistinguishable for the various nanogap sizes (Figs. 6.7c, d). Interestingly, from the plasmonic perspective, the light polarized along the ruler's longitudinal mode should, in principle, deliver the highest

sensitivity to the nanogap size (Fig. 6.7c, *s*-long). However, it is clear that, magnetoplasmonically, the mutual orientation of the electric field of light and the magnetization has much greater significance. Note that, in all panels of Figures 6.7 and 6.8, we also plot the Kerr polarization rotation spectra for a simple nanodisk array (dotted data) in order to give a side-to-side comparison. In this way, an immediate visual sense of how much the ruler response is altered compared to a nanodisk antenna for each gap size can be obtained.

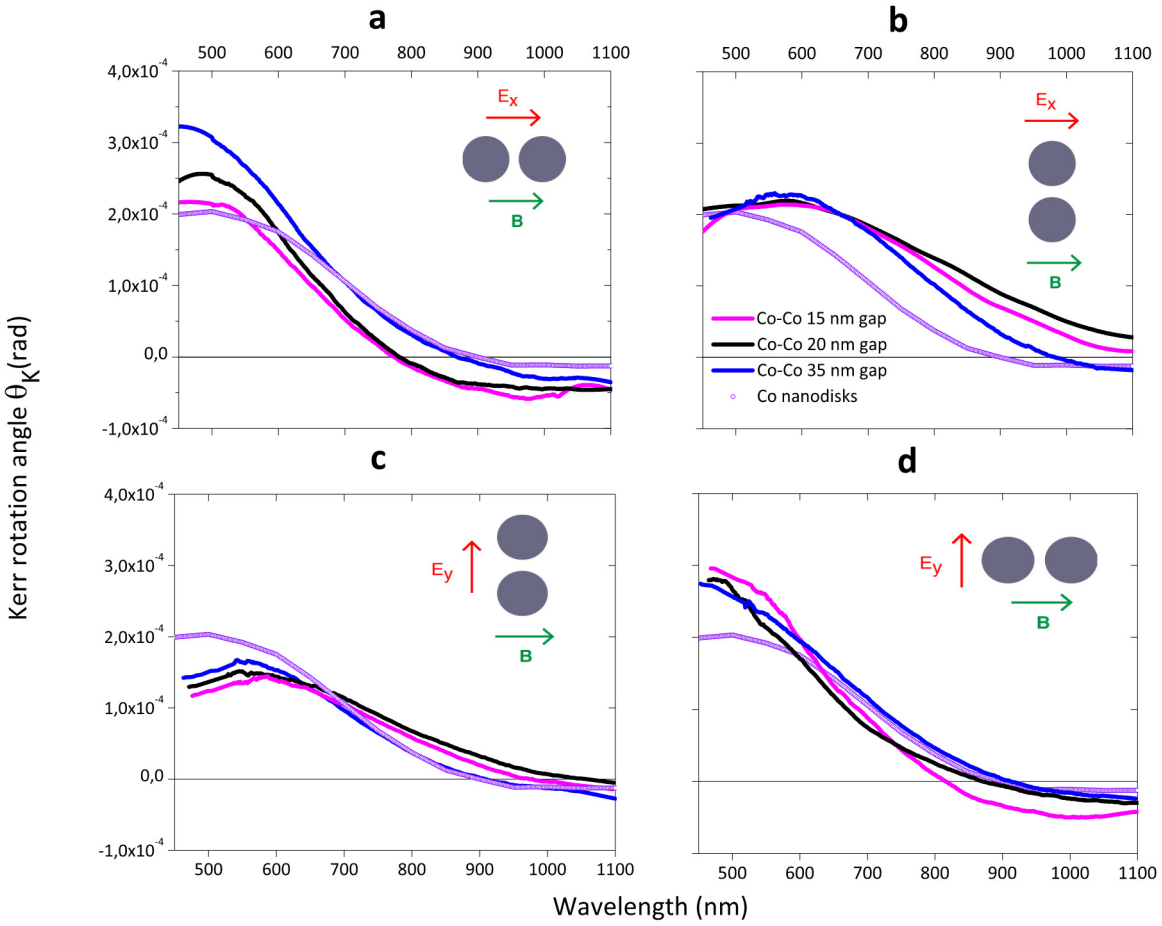

Figure 6.8. Kerr rotation Θ_K spectra of Co rulers with 15 nm, 20 nm, and 35 nm gaps and single Co nanodisks for the respective L-MOKE configurations illustrated in Figure 6.6.

In Fig. 6.9 we demonstrate that the magnetoplasmonic ruler delivers excellent accuracy in nanogap resolution for 10-30 nm regime over the entire visible spectral range, as evidenced by the error bars that result from the calculated standard deviation of multiple spectral scans. This kind of statistical analysis models realistic solution-based plasmon ruler systems and provides a reliable test of the robustness of the nanogap probing with the MOKE.

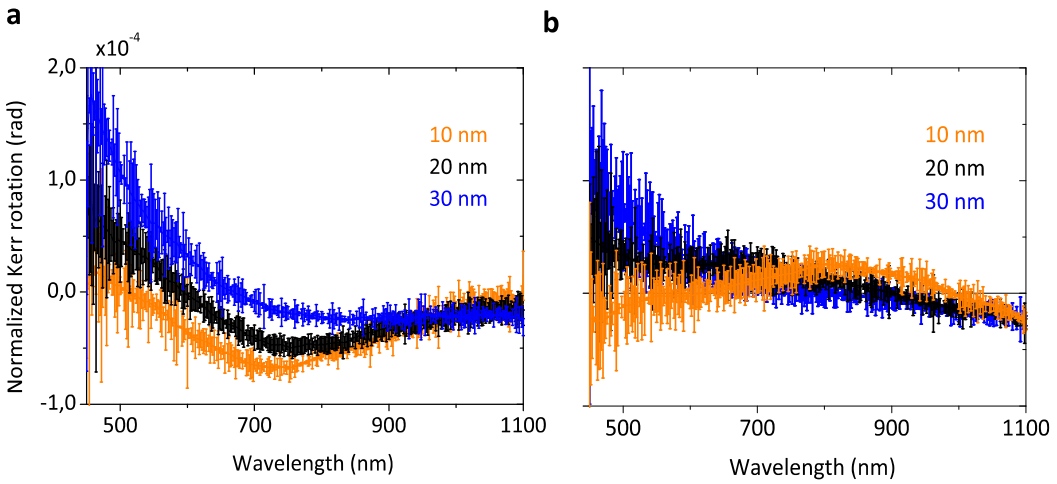

Figure 6.9. Normalized Kerr rotation with error bars for rulers with three nanogaps – 10 nm, 20 nm and 30 nm.

6.6 Analytical calculations of MOKE response.

We perform analytical calculations of the MOKE response (Fig. 6.10) and find an overall agreement between the analytical model and experimentally obtained Kerr polarization rotation spectra in both *p*-long (compare Figs. 6.7a and 6.10a) and *p*-short (Figs. 6.7b and 6.10b) configurations.

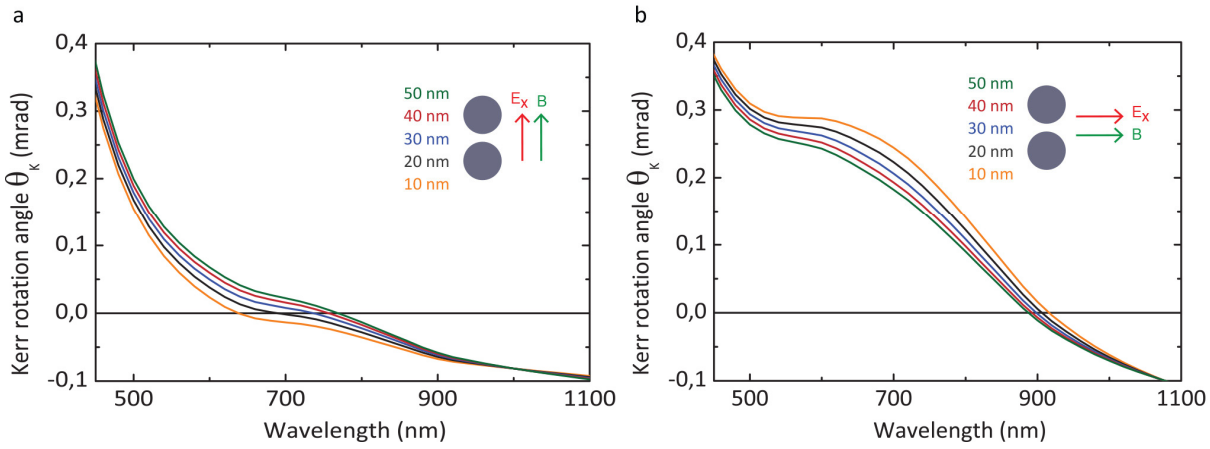

Figure 6.10. Calculated spectral Kerr polarization rotation in Ni rulers with 10 nm, 20 nm, 30 nm, 40 nm and 50 nm gaps for L-MOKE in p-polarization case: *p*-long (a) and *p*-short (b) configurations.

6.7 Evolution of the 'perfect ruler' and its figure-of-merit

We now turn to highlighting the *active operation mode* that is an intrinsic feature of the magnetoplasmonic ruler. Figure 6.11 follows the sequence of spatial orientations of the ruler with respect to the applied magnetic field. From all the spectroscopic MOKE data, we select the spectral region of 625–635 nm since it contains the most common laser lines in single-wavelength MOKE experiments (see the insets in Figs. 6.11 a–c). We see that the rulers at intermediate angles (45° in the *p*-45 case in Fig. 6.11a and 90° in the *p*-short case in Fig. 6.11b), though capable of resolving the nanogap excellently in some spectral regions, fail to do so reliably in the selected most affordable spectral range (see the insets of Figs. 6.11a, b). The most stable configuration of the ruler—i.e., p-long (Fig. 6.11c), which it would potentially adopt in solution by aligning its easy magnetization axis (the longitudinal axis of the ruler) for magnetic fields above magnetic saturation—shows a remarkable resolution of the nanogaps' size up to 40 nm (see the inset of Fig. 6.11c).

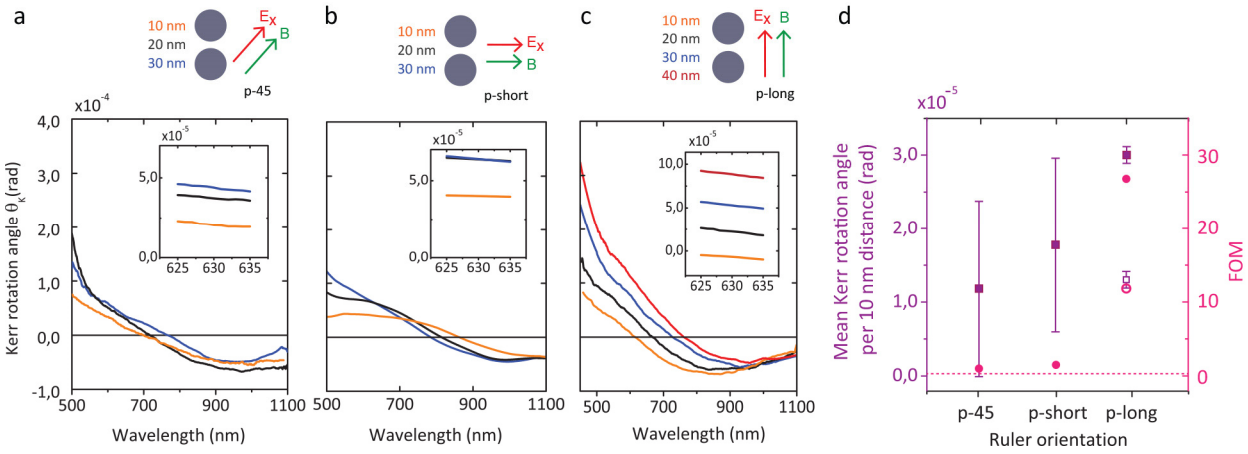

Figure 6.11. Evolution of the 'perfect ruler' and its figure-of-merit. Kerr polarization rotation angle from magnetoplasmonic rulers, with electric and magnetic fields oriented at 45° (*p*-45) (a), along the tangential ruler axis (*p*-short) (b) and along the longitudinal ruler axis (*p*-long) (c). Insets in (a–c): corresponding zoomed views into the 625–635 nm spectral region. (d) Mean Kerr rotation per 10 nm for the three configurations (*p*-45, *p*-short and *p*-long) (left axis) and the corresponding FOMs (right axis). Dotted line: FOM of the plasmon rulers, estimated from [40] and [47].

This is summarized in Fig. 6.11d (left axis), where all three orientations of the ruler are compared against the mean Kerr rotation per 10 nm distance in the nanogap. Both

higher absolute rotations per distance and the smallest error in mean rotation variation in 10-40 nm nanogap regime are achieved here with the *p*-long configured ruler. The latter essentially makes this magnetoplasmonic system a 'perfect ruler' in the conventional sense—that is, a ruler designed to measure both small and large distances with exactly the same precision (see the nearly equidistant Kerr rotation features on the inset of Fig. 6.11c). This becomes clearly visible when we spectrally map the sensitivity of the Kerr polarization rotation angle ($\Delta\Theta_K$) to the distance change of 10 nm (Fig. 6.12), which is practically flat in the 628–633 nm wavelength range.

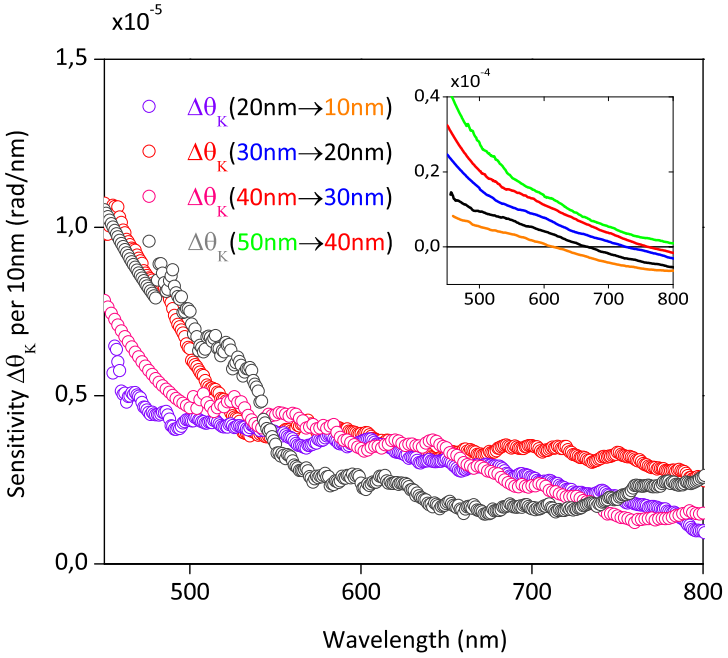

Figure 6.12. Spectrally resolved sensitivity of the ruler as the nanogapis changing by 10 nm from various starting values.

In order to gauge the performance of the regular plasmon and magnetoplasmonic rulers, we define a dimensionless FOM for magnetoplasmonics as the mean change in Kerr polarization rotation angle $\Delta\Theta_K$ induced by a distance change of 10 nm, divided by the standard deviation (SD) of $\Delta\Theta_K$, taken as a measurement precision or the resolution in the MOKE experiment (similar to the full-width-half-maximum (FWHM) of the plasmon peak, but conceptually different from the signal-to-noise ratio):

$$FOM = \frac{\langle \Delta\Theta_K \rangle}{SD(\Delta\Theta_K)} \tag{1}$$

Since in this study we introduce a new way of measuring the nanoscale distances – namely, by using phase-sensitive measurements of the Kerr polarization rotation, it is

also crucial to find dimensionless performance indicators that could characterize the new system, and, more importantly, would allow to compare such indicators with previously devised (plasmon) nanorulers. The figure-of-merit (FOM) seems to be one of such dimensionless indicators, as well as the signal-to-noise ratio. In principle, FOM is quite generally defined for an overwhelmingly broad range of devices to gauge their performance to each other. Bringing forward a new type of device, we attempted to define the FOM for this device in such a way we can compare it with the plasmonic analogues. Inevitably, a new FOM definition is needed since the operating principle of this sensor is markedly different from the plasmon rulers. It turns out that the ratio of the Kerr polarization rotation values, taken at different nanogaps, to the standard deviation in the statistics of these values at given nanogaps and given wavelengths, precisely gives the performance indicator that can be described as FOM. That is, the absolute change of a parameter that reacts on various nanogaps, and how reliably can two values of this parameter at two different nanogaps be distinguished (i.e., what is the reliability of the definition of this parameter). In exact analogy to this, in purely plasmonic systems the FOM relates to the shift of the plasmonic resonance, divided by the full-width-half-maximum (FWHM). By contrast, if one would take the standard deviation in the definition of the plasmon peak position, for example, one would rather arrive at the signal-to-noise ratio. Importantly, that the standard deviation, entering our newly introduced FOM definition, is not the same parameter as the measurement error in itself as we show it by error bars in Figure 6.9, and rather indicates the variation from the mean value of Kerr rotation in the wavelength range 628–633 nm. It is worth to note here that by no means we claim that the presented FOM definition for magnetoplasmonic rulers is the only imaginable one. We merely attempt to start a productive discussion on this issue in the community by putting forward our findings. Similar discussion has already started regarding the definition of FOM in the plasmonic sensing, in particular its definition for small volumes / surfaces, where plasmonic sensors naturally perform the best (see, for example, our own recent take on this with magnetoplasmonic sensing systems in [15] or in this very recent work by the group of Prof. Pol Van Dorpe - Jiaqi Li et al., Revisiting the Surface Sensitivity of Nanoplasmonic Biosensors, *ACS Photonics* 2, 425 (2015). Finally on this point, we would like to stress that our FOM definition and the numbers we're putting forward are rather conservative, as compared, for example, to already mentioned above work on magnetoplasmonic sensing that uses the same measurement principle as the current work, where truly record-breaking numbers are achieved in terms of FOM.

Tracking the FOM values in the range of wavelengths 628–633 nm for all ruler orientations conservatively in the 10-30 nm nanogap regime (pink data points and the right axis of Fig. 6.11d) and comparing these to the highest of previously estimated FOMs for the regular plasmon rulers (~0.62, marked with a dotted line in Fig. 6.11d), we see that not only do the FOMs of magnetoplasmonic rulers in basically any orientation exceed those of the regular plasmon rulers (the *p*-45 orientation gives a FOM of 1.0 and the *p*-short gives a FOM of 1.5), but that, with both electric field and magnetization aligned along the longitudinal axis of the magnetoplasmonic ruler—*i.e.*, the *p*-long orientation—the FOM in measuring nanoscopic distances in 10-30 nm regime reaches 26.7, which exceeds the performance of regular plasmon rulers by roughly two orders of magnitude (Fig. 6.11d, right axis). Extending it to 10-40 nm range (as in Fig. 6.11c), we earn FOM of 12 (open symbols in Fig. 6.11d). As we continue to add larger distances, naturally, the sensitivity of the ruler drops, alongside with increasing standard deviation in Kerr polarization rotation measurements due to nanofabrication particularities of the nanodimers with such large nanogaps by HCL (see Fig. 6.13), where the lateral separation of individual rulers essentially becomes smaller than the nanogap. Still, even in 10-50 nm regime the FOM of magnetoplasmonic ruler reaches 5, an order of magnitude exceeding the regular plasmon rulers. Note that at 60 nm gap the ruler essentially transforms into a collection of individual nanodisks as longitudinal and transversal modes spectrally coincide (Fig. 6.13).

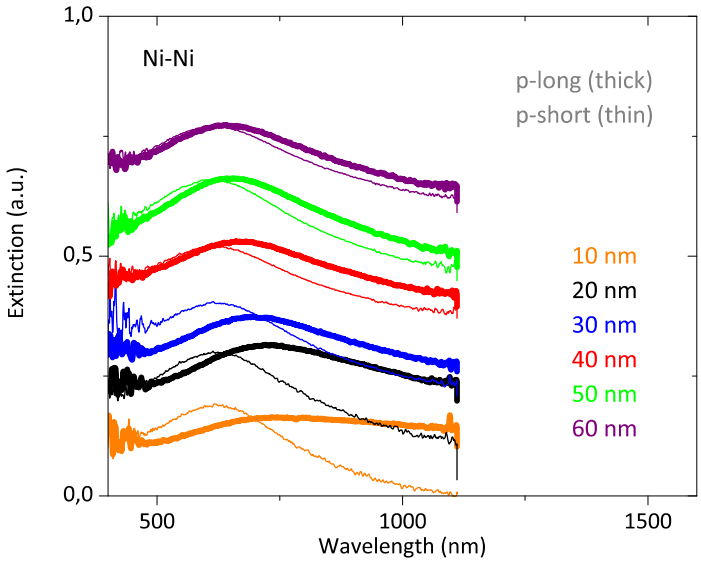

Figure 6.13. Extinction spectra of Ni rulers showing both longitudinal (p-long) and transversal (p-short) modes.

Chapter 7

7 Potential for the magnetoplasmonic ruler in solutions

Apart from the potential intrinsic ability to realign itself during the measurements (for example, in a liquid environment) to adopt the best possible signal resolution and FOM, a situation where the application of the magnetic field at saturation does not readily reorient the ruler can be envisaged. For example, this could be realized in strongly viscous environments or when the ruler is bound to a certain molecular structure. In this case, increasing the magnetic field and simultaneously probing the ruler's spectral polarization rotation response would track the spatial reorientation of the ruler in real time, which would eventually reach its fully aligned configuration. In this scenario, several physical parameters of the embedding medium could be probed, apart from the nanogap reading. These might include the characterization of its viscosity and the various tensile stresses a biochemical system might experience, possibly also providing hints on the dynamic evolution of the structure and the composition. The possibility for the encapsulation of Ni with Au prompts us to envision the scenario of the practical use of the active magnetoplasmonic ruler, where a thin Au layer is created at the surface of metal ferromagnetic nanoparticles, similarly to already widely employed core–shell gold–ferromagnetic oxide theranostic agents. Another Ni biofunctionalization protocol suggesting polyhistidine peptides as purifying agents [55] may also be foreseen. In the envisaged use of magnetoplasmonic rulers in solution, both nanoparticles in the ruler would acquire a magnetic moment with the application of the external magnetic field and would experience attractive forces due to the magnetic dipolar interaction, subjecting the (bio)matter in the ruler gap to mechanical stress by actuation. The attractive force will also be strongest (from pN up to nN) when the ruler reaches the "perfect" orientation. By proper magnetoplasmonic ruler design, magnetic field-induced orientation and mechanical actuation would be used simultaneously to implement a conceptual device for the nanocharacterization of the elastoplastic properties of soft matter. This would allow probing of multidimensional length variations in molecular systems with subnanometer precision under the application of precisely controlled

external stimuli. In practice, the field control of the force exerted by the nanoparticles in the ruler can be readily achieved by using systems with magnetic moment proportional to magnetic field. This could be realized in various ways, for example, by using nanostructures made of a Py (permalloy)/Cu/Co trilayer. By tuning the Cu spacer thickness, the Py and Co nanodisks could be antiferromagnetically exchange-coupled in each element of the ruler at zero field, giving a net zero magnetic moment [56, 57]. This means that the material inside the ruler gap would experience no mechanical stress. As the external magnetic field is ramped up, the two magnetic submoments in each element of the ruler would rotate in opposite direction, such that the angle between them progressively changes from 180° to 0°, leading to a total magnetic moment proportional to the applied field, and precisely controlled by it. Such magnetic moment induction then translates to mechanical stress in the ruler gap, which is in turn precisely controlled by the external magnetic stimuli. Another alternative is use simple Py nanodisk elements that can be individually designed to form a so-called magnetic vortex state. In this case too, in the absence of an externally applied magnetic field, the magnetic moment of each nanodisk is negligibly small, and it is only when the field is applied that a magnetic moment proportional to magnetic field is induced by the distortion of the vortex configuration [58]. This second approach implies the use of much simpler ruler structures; however, the moment induced in the nanodisk units is much smaller (in the linear regime, i.e. where $\mu \sim H$ than that achievable through multilayered ruler elements. In principle, this difference can be turned into an advantage, as it implies that a spectrum of opportunities exists from which to devise a nanoscale elastoplastic molecular characterization tool, designed by selecting the proper ruler structure and depending on the required force range. Importantly, neither design affects the core magnetoplasmonic ruler principle of nanoscale distance measurement, discussed above.

In general, it appears that the potential extension of the active magnetoplasmonic ruler concept to colloidal nanoparticles in a biological environment is within the practical reach. Besides the scenarios we described above, the assembly of nanoparticles in solution can now be guided by light with precisely controlled separations [59]. Further, a very recent study on magnetic hydrogel for clinic applications demonstrates how colloidal magnetic nanoparticles, suspended in a hydrogel, are controllably organized in chains with alternating magnetic field [60]. With already mentioned bulk of studies on the biocompatibility of magnetic nanoparticles, and the availability of various core-shell geometries, accommodating the ferromagnetic functionalities also with the possibility of direct biofunctionalization of the ferromagnetic metallic nanostructures, we overall expect the magnetoplasmonic rulers to meet similar challenges as their plasmonic

counterparts. That is, the exact positioning / delivery and optical signal read-out, often obstructed by the strong absorption in biological media, would be the issues to address for both types of rulers. However, magnetoplasmonic rulers deliver the clear advantage of the active operation, outlined above, which can also be employed to solve the mentioned challenges, for example, with precision delivery.

Chapter 8

8 Summary and Outlook

In this thesis, we introduce magnetoplasmonics for the ultrasensitive optical measurements of the nanoscale distances. We develop a new type of a magnetic field-activated plasmon ruler that reports nanogap distances via Kerr polarization rotation. The features of this system include its robustness in nanogap measurements over a broad spectral range, the capacity to report both small and larger nanoscale distances with about two orders of magnitude better FOM than regular plasmon rulers, and its intrinsic ability to adopt the spatial orientation best suited for the nanogap measurements, something we call *signal amplification by spatial orientation*. All these features are realized in a highly parallel fashion; that is, all magnetoplasmonic rulers of the measured ensemble would necessarily adopt a nominally identical orientation. This allows us to envision such rulers being employed not only for highly sensitive determination of nanoscale distances but also as versatile nanotools for characterizing soft matter by dynamically tracking the elastic and other physical properties of various biological and chemical media. Future work includes possible realization of the magnetoplasmonic nanorulers systems in aqueous solutions along with biologically relevant molecular species.

Another route is to design solid-state light polarization-control systems, based on these basic nanoantennas. Indeed, magnetoplasmonic rulers represent an archetypical dimer plasmon antenna configuration, with reasonably large near-field enhancement and magnetic-field-controlled light polarization rotation. Introducing the structural asymmetry (in size and/or shape of the nanodisks) in such nanodimer antenna might give further access to higher-quality hybrid Fano-type resonances. In these magnetoplasmonic nanoantennas such resonances would be combined then with the tunability by the external magnetic field. The dimer nanoantennas are produced on a macroscale with highly parallel bottom-up nanofabrication, potentially forming large-scale adaptive optical metasurfaces.

Acknowledgements

I am grateful to have many good people around and here I would like to thank the ones who have made this thesis possible:

My supervisor Alexander Dmitriev- thank you for providing me the opportunity to be a PhD student in your small but powerful group, for all inspiring ideas and passion in science you always share, for your valuable guidance and always being available no matter where you are.

Kristof Lodewijks- thank you for introducing me to MOKE and helping out with ellipsometry measurements, and also for sharing your huge experience on nanofabrication, optics and plasmonics. I wish you best of luck with your position as photonics design engineer at IMEC and future research.

Paolo Vavassori and Nicolò Maccaferri- thank you for our nice collaboration and team work and for sharing your huge knowledge on magneto-optics. Nicolò- thank you for kindly providing all analytical models used in this thesis.

Randy K. Dumas- thank you for introducing me to alternating gradient magnetometry, for providing me high-quality magnetic films and for sharing your broad knowledge on nanomagnetism and magnetic materials.

Addis Mekonnen –thank you for all exciting discussions and sharing your passion in physics, for helping me out with measurements and for sharing your expertise in magnetism and optics.

Mats Hagberg and Henrik Frederiksen- I am grateful for all your help with evaporation tools in the cleanroom and always being nice and helpful.

Mojtaba- thank you for all nice collaboration and fun moments we had, and good luck with your professor position at University of California, Riverside.

Vladimir Miljković- thank you for introducing me to HCL and nanofabrication of dimers.

Gülis Zengin-thank you for introducing me to scanning electron microscopy and always being nice and friendly.

Virginia Claudio- thank you for introducing me to ion beam milling and for all nice discussions we had.

Yuli, Masoumeh, Martina, Mohammad and Afshin in Johan Åkerman's group for being such a nice lab mates.

Last but not least, a huge thanks to my lovely parents for their endless love, care and support through my life and my parents-in-law, Ann-Marie and Hasse, - it's a great pleasure in being a part of your family. Jakob, you are an essential part of my life and I am grateful for all time we have together.

Finally, I would like to acknowledge the Swedish Foundation for Strategic Research (SSF) Future Research Leader Grant.

.

References

1. Maier, S.A., *Plasmonics : fundamentals and applications*. 2007, New York: Springer. xxiv, 223 p.
2. Maier, S.A., *Plasmonics: Fundamentals and Applications.* 2007.
3. Gaponenko, S.V., *Introduction to nanophotonics*. 2010, Cambridge: Cambridge University Press. xviii, 463 s.
4. Armelles, G., et al., *Magnetoplasmonics: Combining Magnetic and Plasmonic Functionalities.* Advanced Optical Materials, 2013. **1**(1): p. 10-35.
5. Armelles, G. and A. Dmitriev, *Focus on magnetoplasmonics.* New Journal of Physics, 2014. **16**(4): p. 045012.
6. Temnov, V.V., et al., *Active magneto-plasmonics in hybrid metal–ferromagnet structures.* Nature Photonics, 2010. **4**(2): p. 107-111.
7. Belotelov, V.I., et al., *On surface plasmon polariton wavepacket dynamics in metal-dielectric heterostructures.* J Phys Condens Matter, 2010. **22**(39): p. 395301.
8. Temnov, V.V., *Ultrafast acousto-magneto-plasmonics.* Nature Photonics, 2012. **6**(11): p. 728-736.
9. Temnov, V.V., et al., *Femtosecond nonlinear ultrasonics in gold probed with ultrashort surface plasmons.* Nat Commun, 2013. **4**: p. 1468.
10. Pohl, M., et al., *Tuning of the transverse magneto-optical Kerr effect in magneto-plasmonic crystals.* New Journal of Physics, 2013. **15**(7): p. 075024.
11. Gonzalez-Diaz, J.B., et al., *Plasmonic Au/Co/Au nanosandwiches with enhanced magneto-optical activity.* Small, 2008. **4**(2): p. 202-5.
12. Maccaferri, N., et al., *Tuning the Magneto-Optical Response of Nanosize Ferromagnetic Ni Disks Using the Phase of Localized Plasmons.* Physical Review Letters, 2013. **111**(16).
13. Bonanni, V., et al., *Designer magnetoplasmonics with nickel nanoferromagnets.* Nano Lett, 2011. **11**(12): p. 5333-8.
14. Stipe, B.C., et al., *Magnetic recording at 1.5 Pb m−2 using an integrated plasmonic antenna.* Nature Photonics, 2010. **4**(7): p. 484-488.
15. Maccaferri, N., et al., *Ultrasensitive and label-free molecular-level detection enabled by light phase control in magnetoplasmonic nanoantennas.* Nat Commun, 2015. **6**: p. 6150.

16. Zubritskaya, I., et al., *Active magnetoplasmonic ruler.* Nano Lett, 2015. **15**(5): p. 3204-11.
17. Griffiths, D.J., *Introduction to electrodynamics*. 3rd ed. 1999, Upper Saddle River, N.J.: Prentice Hall. xv, 576 p.
18. Novotny, L. and B. Hecht, *Principles of nano-optics*. 2006, Cambridge ; New York: Cambridge University Press. xvii, 539 p.
19. Hecht, E., *Optics*. 4. ed. 2002, San Francisco, Calif.: Addison Wesley. 698 s.
20. Johnson, P.B. and R.W. Christy, *Optical Constants of the Noble Metals.* Physical Review B, 1972. **6**(12): p. 4370-4379.
21. Bohren, C.F. and D.R. Huffman, *Absorption and scattering of light by small particles*. 1983, New York: Wiley. xiv, 530 p.
22. Nordlander, P.O., C.; Prodan, E.; Li, K.; Stockman, M. I. , *Plasmon Hybridization in Nanoparticle Dimers.* Nano Letters, 2004. **4**: p. 899–903.
23. Prodan, E., et al., *A hybridization model for the plasmon response of complex nanostructures.* Science, 2003. **302**(5644): p. 419-22.
24. Reinhard, B.M., et al., *Use of plasmon coupling to reveal the dynamics of DNA bending and cleavage by single EcoRV restriction enzymes.* Proc Natl Acad Sci U S A, 2007. **104**(8): p. 2667-72.
25. Zvezdin, A.K. and V.A. Kotov, *Modern magnetooptics and magnetooptical materials*. Studies in condensed matter physics. 1997, Philadelphia, Pa.: Institute of Physics Pub. xviii, 386 s.
26. Faraday, M., *Experimental Researches in Electricity. Nineteenth Series.* Philosophical Transactions Royal Society London, 1846. **136**.
27. Smith, D.A. and K.L. Stokes, *Discrete dipole approximation for magneto-opticalscattering calculations.* Optics Express, 2006. **14**(12): p. 5746-5754.
28. Xia, T.K., P.M. Hui, and D. Stroud, *Theory of Faraday rotation in granular magnetic materials.* Journal of Applied Physics, 1990. **67**(6): p. 2736.
29. Chen, J., et al., *Plasmonic nickel nanoantennas.* Small, 2011. **7**(16): p. 2341-7.
30. Sepúlveda, B., et al., *Plasmon-Induced Magneto-Optical Activity in Nanosized Gold Disks.* Physical Review Letters, 2010. **104**(14).
31. Pineider, F., et al., *Circular magnetoplasmonic modes in gold nanoparticles.* Nano Lett, 2013. **13**(10): p. 4785-9.
32. Banthi, J.C., et al., *High magneto-optical activity and low optical losses in metal-dielectric Au/Co/Au-SiO(2) magnetoplasmonic nanodisks.* Adv Mater, 2012. **24**(10): p. OP36-41.

33. de Sousa, N., et al., *Interaction effects on the magneto-optical response of magnetoplasmonic dimers.* Physical Review B, 2014. **89**(20).
34. Armelles, G., et al., *Mimicking electromagnetically induced transparency in the magneto-optical activity of magnetoplasmonic nanoresonators.* Optics Express, 2013. **21**(22): p. 27356.
35. González-Díaz, J.B., et al., *Cobalt dependence of the magneto-optical response in magnetoplasmonic nanodisks.* Applied Physics Letters, 2010. **97**(4): p. 043114.
36. Maccaferri, N., et al., *Effects of a non-absorbing substrate on the magneto-optical Kerr response of plasmonic ferromagnetic nanodisks.* physica status solidi (a), 2014. **211**(5): p. 1067-1075.
37. Maccaferri, N., et al., *Polarizability and magnetoplasmonic properties of magnetic general nanoellipsoids.* Opt Express, 2013. **21**(8): p. 9875-89.
38. Lodewijks, K., et al., *Magnetoplasmonic design rules for active magneto-optics.* Nano Lett, 2014. **14**(12): p. 7207-14.
39. Sonnichsen, C., et al., *A molecular ruler based on plasmon coupling of single gold and silver nanoparticles.* Nat Biotechnol, 2005. **23**(6): p. 741-5.
40. Hill, R.T.M., J. J.; Hucknall, A.; Wolter, S. D.; Jokerst, N. M.; Smith, D. R.; Chilkoti, A., *Plasmon Ruler with Angström Length Resolution.* ACS Nano 2012. **6**: p. 9237–9246.
41. Prashant, K.J.H., W.; A. El-Sayed, M. , *On the Universal Scaling Behavior of the Distance Decay of Plasmon Coupling in Metal Nanoparticle Pairs: A Plasmon Ruler Equation.* Nano Letters, 2007. **7**: p. 2080–2088.
42. Na Liu, L.H., M.; Weiss, T.; Alivasatos, A. P.; Giessen, H., *Three-Dimensional Plasmon Rulers.* Science, 2011. **332**: p. 1407–1410.
43. Rechberger, W., et al., *Optical properties of two interacting gold nanoparticles.* Optics Communications, 2003. **220**(1-3): p. 137-141.
44. Wang, J.B., S. V.; Wang, H.; Reinhard, B. M., *Illuminating Epidermal Growth Factor*
Receptor Densities on Filopodia through Plasmon Coupling. ACS Nano 2011. **5** p. 6619–6628.
45. Anker, J.N.H., W. P.; Lyandres, O.; Shah, N. C.; Zhao, J.; Van Duyne, R. P. , *Biosensing with plasmonic nanosensors.* Nature Materials, 2008. **7** p. 442–452.
46. Sheikholeslami, S., et al., *Coupling of optical resonances in a compositionally asymmetric plasmonic nanoparticle dimer.* Nano Lett, 2010. **10**(7): p. 2655-60.

47. Acimovic, S.S.K., M. P.; González, M. U.; Quidant, R. , *Plasmon Near-Field Coupling in Metal Dimers as a Step toward Single-Molecule Sensing.* ACS Nano 2009. **3**: p. 1231–1237.
48. Gunnarsson, L.R., T.; Prikulis, J.; Kasemo, B.; Käll, M.; Zou, S.; Schatz, G. C. , *Confined Plasmons in Nanofabricated Single Silver Particle Pairs: Experimental Observations of Strong Interparticle Interactions.* J. Phys. Chem. B. , 2005. **109** p. 1079–1087.
49. Kuzyk, A., et al., *Reconfigurable 3D plasmonic metamolecules.* Nat Mater, 2014. **13**(9): p. 862-6.
50. Fredriksson, H., et al., *Hole–Mask Colloidal Lithography.* Advanced Materials, 2007. **19**(23): p. 4297-4302.
51. Vavassori, P., *Polarization modulation technique for magneto-optical quantitative vector magnetometry.* Applied Physics Letters, 2000. **77**(11): p. 1605.
52. Oakberg, T., *Magneto-optic Kerr Effect application note*, in *Hinds Instruments*. 2010.
53. Ctistis, G.P., E.; Patoka, P.; Gutek, J.; Fumagalli, P.; Giersig, M., *Optical and Magnetic Properties of Hexagonal Arrays of Subwavelength Holes in Optically Thin Cobalt Films.* Nano Letters, 2009. **9**: p. 1-6.
54. Dmitriev, A., *Nanoplasmonic sensors*. Integrated analytical systems. 2012, New York, NY: Springer. x, 394 p.
55. Hochuli, E.B., W.; Döbeli, H.; Gentz, R. & Stüber, D. , *Genetic Approach to Facilitate Purification of Recombinant Proteins with a Novel Metal Chelate Adsorbent.* Nature Biotechnology 1988. **11**: p. 1321–1325.
56. Bonanni, V., et al., *Shape and thickness effects on the magnetization reversal of Py/Cu/Co nanostructures.* Journal of Magnetism and Magnetic Materials, 2009. **321**(19): p. 3038-3041.
57. Bonanni, V.U.d.F.M.S.D.C.-I.N.R.C.U.o.I.a.C.P.A.o.S.C.U.B., A; Grimsditch, M; Ilic, B; Lebecki, K. M; CIC nanoGUNE Consolider; Metlushko, V; Vavassori, P. Bisero, D *Magnetostatic dipolar domain-wall pinning in chains of permalloy triangular rings.* Phys. Rev. B, 2008. **78**(17).
58. M. Grimsditch, P.V., V. Novosad, V. Metlushko, H. Shima, Y. Otani, and K. Fukamichi, *Vortex chirality in an array of ferromagnetic dots.* Phys. Rev. B, 2002. **65**: p. 172419.
59. Herrmann, L.O., et al., *Threading plasmonic nanoparticle strings with light.* Nat Commun, 2014. **5**: p. 4568.

60. Hu, K., et al., *A novel magnetic hydrogel with aligned magnetic colloidal assemblies showing controllable enhancement of magnetothermal effect in the presence of alternating magnetic field.* Adv Mater, 2015. **27**(15): p. 2507-14.